Ligand shell morphology of water-soluble mixed-monolayer protected gold nanoparticles

by Suelin Chen

B.S. Biology
Minors in Biomedical Engineering and Music
Massachusetts Institute of Technology, 1999

Submitted to the Department of Materials Science and Engineering in partial fulfillment of the requirements for the degree of

MASTER OF SCIENCE IN MATERIALS SCIENCE AND ENGINEERING

at the

MASSACHUSETTS INSTITUTE OF TECHNOLOGY

June 2007

Signature of Author: _____
Department of Materials Science and Engineering
May 10, 2007

Certified by: _____
Francesco Stellacci
Finmeccanica Assistant Professor of Materials Science and Engineering
Thesis Supervisor

Accepted by: _____
Samuel M. Allen
POSCO Professor of Physical Metallurgy
Chair, Departmental Committee on Graduate Students

Acknowledgements.

I would first like to thank my advisor, Francesco Stellacci, who has guided my research and whom I greatly admire for his creativity, intelligence, and unbridled enthusiasm for science.

I am indebted to Alicia Jackson, Ying Hu, and Cedric Dubois for their imaging expertise and sage advice. Special thanks to Alicia Jackson for her discovery of rippled nanoparticles which makes this research possible. I would also like to thank Oktay Uzun and Ayush Verma for the synthesis of molecules and nanoparticles that were integral to my project. I have met many wonderful people in SuNMaG, but I would like to especially thank Ozge Akbulut, Sarah Thevenet, and Brenda Long for being amazingly supportive friends—they are three of the most amazing women I have ever met.

Thanks to the Department of Materials Science and Engineering at MIT for believing that an ambitious biology student could hack it in engineering. They have given me the opportunity to fulfill my dream of using my unique viewpoint to make a novel contribution to the field of materials science. My journey in graduate school has been difficult at times but I am proud to have come this far and I hope to continue to use my special set of skills to do some exciting interdisciplinary research.

Thanks to Mat Laibowitz for giving me something to look forward to after imaging at the STM and for talking some sense into me.

I am also grateful to the music, dance, and visual arts communities at MIT that have provided a much needed therapeutic outlet for me.

Last but certainly not least, a huge thanks to my incredibly supportive family and their bottomless well of encouragement. My parents are the best parents in the world and I am incredibly lucky to have them.

Table of Contents.

Table of Figures.

Ligand shell morphology of water-soluble mixed-monolayer protected gold nanoparticles.

1 Abstract

Nanoparticles comprise a versatile class of nanomaterials that consist of particles that have a characteristic length scale less than 100nm. They are on a similar length scale as many biological elements, so it is fitting that they are being used increasingly in biological systems for a variety of applications. Interesting properties of water-soluble metal nanoparticles that could lead to novel biological applications include bio-catalytic,[1,2] sensing,[3] and light scattering[4] capabilities.

We will present here the characterization of novel highly water-soluble gold nanoparticles that can be used as model systems to study the fundamental mechanisms of cellular uptake and intracellular trafficking.

2 Background

2.1 Background: History of metal nanoparticles

Metal nanoparticles have already been used in a variety of applications, and their use will certainly continue to be an important area of research in the coming years. Their utility lies in fields ranging from materials science to biology, chemistry to electronics.

People have been using metal nanoparticles for centuries. In earlier times metal nanoparticles were often used for optical properties: for example, the famous Lycurgus cup (Figure 1) from 4-5th century B.C. shines red in transmitted light and green in reflected light,[5] the coated gold colloid Purple Cassius was used to color glassware and enamel in the 17th century, and stained glass colored as a brilliant ruby was also used around this time period. In all these cases, the intense color is due to the presence of colloidal gold particles,[6] their color determined by the diameter, shape, and concentration of the particles. The specific nature of these colloids was only elucidated by Michael Faraday much later in 1857, who had been studying the optical nature of various metals, and especially gold, for several years. Faraday referred to these colloidal metals as "divided metals" and many believe his work marks the beginning of modern colloid science.

Figure 1. Lycurgus cup, which appears to be red when light shines from within the cup (transmitted) and green when light shines onto the cup (reflected). Adapted from ref [5].

In the 20th century, a better understanding of colloidal gold led to different types of syntheses. One of the conventional syntheses for gold nanoparticles, as introduced by Turkevitch et al in 1951 and refined by Frens et al. in 1970, involved a citrate reduction of $HAuCl_4$ in water, which leads to nanoparticles of about 20 nm in diameter. These electrostatically-stabilized nanoparticles can irreversibly aggregate, making further handling and manipulation difficult to impossible.[7] Schmid and co-workers produced smaller, highly monodisperse gold nanoparticles using a synthesis for $Au_{55}(PPh_3)_{12}Cl_6$, which consists of a phosphine-stabilized gold core made up of a "magic number" (discussed in section 2.2.2) of gold atoms.[8] Their unique size-dependent properties were studied in great detail but their applications were limited because their highly energetic surfaces caused them to be thermally unstable, decomposing at about 50–60°C.

2.2 Background: Monolayer-protected gold nanoparticles

A more robust and versatile version of nanoparticle synthesis was introduced by Brust, Schiffrin and coworkers in their seminal paper describing the synthesis of the first stable monolayer-protected gold nanoparticles[9] (synthesis discussed in section 2.2.1), thus opening a host of new possibilities in nanoscience. Monolayer-protected gold nanoparticles are particularly of interest because of their stability in air, their ability to be dispersed in various solvents without irreversible aggregation, and their small dimension.[10] They consist of a metallic nanocrystal coated by a self-assembled monolayer (SAM) of thiolated molecules (Figure 2), which serves many functions, including being a barrier to non-specific aggregation. Gold nanoparticles are particularly appealing because thiol-gold chemistry is well understood and a large variety of molecules can be placed on the core of these nanoparticles.[11] Furthermore, the synthesis of these nanoparticles is relatively simple,[10] and ligands can be placed in the shell either via place-exchange reactions or by synthesizing the nanoparticle directly with the desired

ligand. The specific properties of a nanoparticle—including its solubility,[12] its electro-optical behavior[13] and its catalytic[2] behavior—is largely determined by the ligand shell, so it is advantageous to be able to control what molecules are in the ligand shell and their relative proportions. The structure of the molecules in the ligand shell is also important, and this report will delve into an investigation of this particular aspect of nanoparticles in great detail.

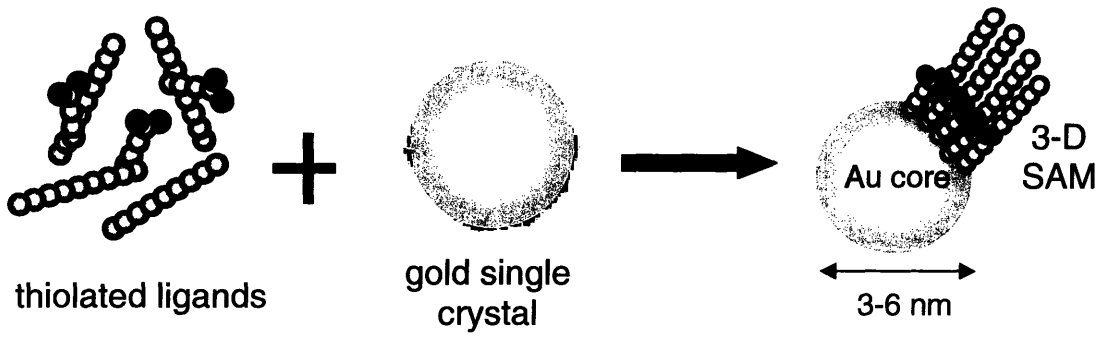

Figure 2: Schematic of thiolated gold nanoparticles.

These monolayer-protected gold nanoparticles typically range in size between 1-10 nm, a size range intermediate between bulk materials and small molecules, and this gives rise to various interesting properties. For example, nanoparticles have a gap between their valence and conduction bands so that size-dependent quantization effects can occur.[10] Furthermore, free electrons can become trapped in the quantum box of the nanoparticle and collectively oscillate, resulting in the plasmon resonance band which is observed at around 530 nm for nanoparticles in the size range relevant to this study.

2.2.1 Synthesis

In 1994 the Brust-Schiffrin method[9] was published, and it has had an enormous influence on the field of gold nanoparticles. This relatively simple synthesis yields gold nanoparticles which are stable in air, have a more monodisperse and controllable size (1.5-5.2 nm), and can be isolated and redissolved in solvents repeatedly without irreversible aggregation. These characteristics allow the nanoparticles to be handled, cleaned and chemically modified as if they were stable compounds.

The nanoparticles discussed in this report are synthesized in the one phase method,[14] which allows a variety of functional thiol molecules to be placed directly on the nanoparticle surface. The diameter of the nanoparticles can be tuned using the thiolate:$AuCl_4$- ratio, with a maximum core diameter of about 5.2 nm.

Place exchange is another way to control the composition of the ligand shell of the nanoparticle, and this mechanism has been studied in great detail by Murray et al. [15,16] The general mechanism is $x(R'SH) + (RS)_mMPC \rightarrow x(RSH) + (R'S)_m(RS)_{m-x}MPC$, where x signifies the number of ligands place-exchanged and m signifies the original number of alkanethiolate ligands per Au_{314} cluster. They found that the kinetics of this process

depend on a variety of parameters, including the ratio of free ligand to bound ligand, their relative bulk, and their relative chain lengths.

Although other ligands such as disulfides[17] and xanthates[18] have been used to stabilize gold nanoparticles, thiols are still the most effective.[10]

2.2.2 Characterization

To view the core of the gold nanoparticle, we use transmission electron microscopy (TEM).[9] TEM gives information on the size of the core, the polydispersity of the nanoparticle population, as well as an idea of the type of shapes formed by the nanoparticles. Core size has also been measured using small-angle X-ray scattering (SAXS),[19],[20] laser-desorption ionization mass spectroscopy,[21] and X-ray diffraction (XRD).[22] Scanning tunneling microscopy (STM) and atomic force microscopy (AFM) can also be used to discern size of the nanoparticle, although unlike TEM their dimensions typically include the molecules in the ligand shell.[19,23] The capability of the STM to discern head groups in the ligand shell will be particularly important in this study, for reasons that I will discuss in section 2.3.

The number of atoms in the gold clusters is determined by the packing of the gold atoms and each atom's number of nearest neighbors; this geometric constraint yields a series of "magic numbers" which correspond to the number of gold atoms in the clusters of our nanoparticles. The number of atoms can be determined by the relation $10n^2 + 2$ with n representing the layer number.[24] Thus, one can theoretically determine the number of atoms from the nanoparticle diameter. For example, a gold nanoparticle approximately 4 nm in diameter would be expected to contain 309 atoms. Of course, the presence of defects will allow nanoparticles with an intermediate number of atoms to exist.

X-ray photoelectron spectroscopy (XPS) can be used to determine the oxidation state of the gold in the nanoparticle[9] and can also determine the average number of thiolated ligands per nanoparticle core.[25] Thermogravimetric analysis (TGA) can also provide information on the number of ligands surrounding the core.[25] In addition, the number of thiolated ligands can then be calculated from the number of gold core atoms and the relative Au/S ratio.[10]

Infrared (IR) and UV-visible (UV-vis) spectra can be used to verify structure and composition of the ligand shell (on a population average basis), along with nuclear magnetic resonance (NMR) spectroscopy.[23] These techniques can also be used to qualitatively measure purity because the peaks of free alkanethiols are less broad than those due to the alkanethiols on the nanoparticle itself. IR spectroscopy has shown that the conformation of the molecules in the ligand shell of the nanoparticle resemble that of molecules in a 2-D SAM;[26] i.e., they are mostly in an all-trans zig-zag conformation with 5-25% gauche defects at both chain ends, with the number of defects increasing with respect to chain length.[19] One reason for the increased number of defects could be the high number of defects in the gold core itself.[27] IR, NMR, and differential scanning calorimetry (DSC) together allow for the study the order-disorder transitions of solid state gold nanoparticles, which is dependent on temperature and chain length.[28]

STM, TEM as well as X-ray diffraction (XRD) have been used to study the amount of order in nanoparticle films, and it has been found that under certain conditions

thiolated gold nanoparticles are able to pack and form highly ordered superlattices with periodicity up to tens of microns in three dimensions.[29]

2.3 Background: Rippled Nanoparticles

It has been shown that when more than one kind of molecule self-assembles into a SAM on a two-dimensional surface, these molecules can phase separate into domains[30] as shown in Figure 3. This of course depends on the structure of the molecules and their relative miscibility. However, these 2-D phase-separated domains do not exhibit any specific order.[30] This phase separation process is a thermodynamically driven process.[31]

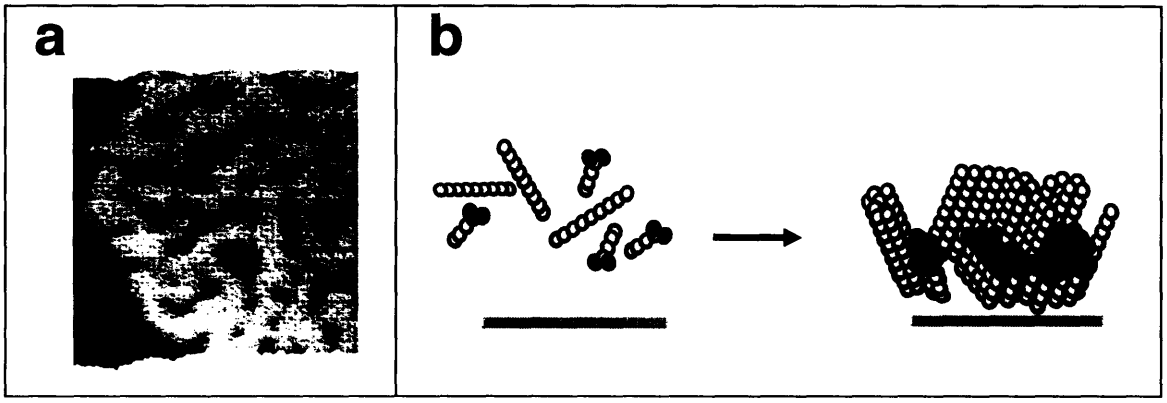

Figure 3: 2-D SAMs. (a) STM height image of phase separated $CH_3O_2C(CH_2)_{15}SH$ and $CH_2(CH_2)_{15}SH$ in a 1:1 ratio on Au (111). Adapted from ref [30]. (b) Schematic of two different molecules self-assembling onto gold to create a 2-D SAM.

When two immiscible molecules are mixed together on a curved surface (as on the surface of a nanoparticle), the curvature of the nanoparticle provides a driving force for further ordering of the domains. The molecular vectors formed by the tilt angle of the 2-D crystalline SAM propagate around the 3-D core,[32] and how these molecules maintain order with the additional constraint of the curvature is still under investigation.

Although the behavior of SAMs on the 3-D surface of the nanoparticle is similar to the behavior of SAMs on a 2-D surface, there are some clear differences in packing. For example, octanethiol monolayers on a flat surface have a headgroup spacing of 5.0 Å, while octanethiol monolayers on a nanoparticle (i.e., octanethiol-coated nanoparticles) display an average headgroup spacing of 5.4 Å which is dependent on the diameter of the nanoparticle.[33] Clearly curvature plays a key role in the organization of ligands on the nanoparticle surface.

Jackson et al. has previously found that when two different molecules are used to form the nanoparticle ligand shell, they will phase separate into highly ordered ribbon-like domains[33,34] as shown in Figure 4. The size of these domains is on the order of ~0.5 nm, an unprecedented ordering length scale. These domains are comparable in size to small molecules, and this can lead to interesting behavior which we will discuss in section 2.3.2. In this section it will become clear that simply knowing the chemical composition of the ligand shell is not sufficient to fully understand the properties of the nanoparticle; the structure of the ligands can also play a role.

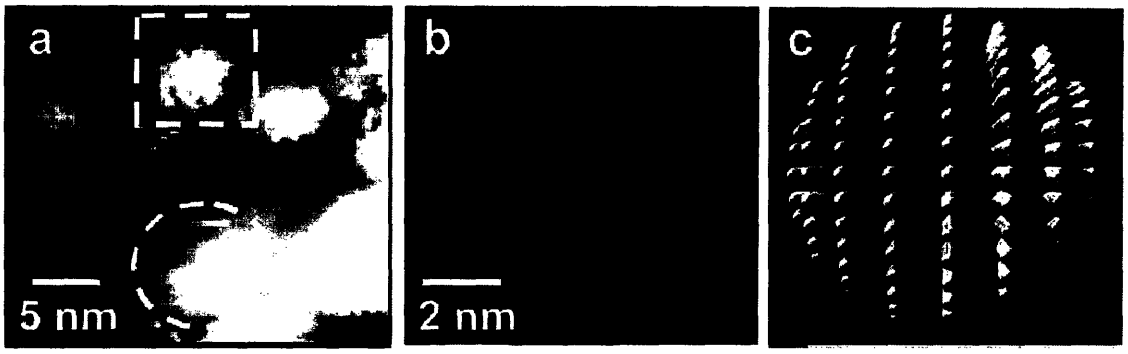

Figure 4: Rippled Nanoparticles. STM height image of OT:MPA 1:2 nanoparticles exhibiting ripples. Dotted box outlines a nanoparticle whose enlarged image is shown in (b), and dotted circle outlines bare gold surface. Note that the bare gold has a similar curvature as the nanoparticles but no ripples are observed, showing that ripples are not solely an imaging artifact of scanning over a region of curvature. (c) Schematic helping to visualize the arrangement of molecules on the nanoparticle surface, where the raised yellow regions are OT. Adapted from ref [33].

Molecular simulation models have been carried out to predict the morphology of domains that mixed ligands will form on nanoparticles and so far they confirm this phenomenon.[35]

2.3.1 Characterization of rippled nanoparticles

Our group investigates the ligand shell morphology in nanoparticles using STM, which can achieve molecular-scale resolution under the proper conditions.[36] STM has the advantage over spectroscopic characterization techniques in that it can provide single-nanoparticle data and not just average properties over large populations of nanoparticles. This is particularly important because our nanoparticle population is inherently polydisperse. STM as a characterization technique is fairly difficult and the analysis is subject to operator discretion, thus one must analyze many images obtained at different conditions to achieve viable data.

In STM (Figure 5), an atomically sharp tip scans the surface while a voltage is applied between the tip and the surface. If the surface is sufficiently conductive, electrons will tunnel from the surface to the tip or vice versa depending on whether the voltage bias is positive or negative. A weak electric current arises from the tunneling electrons, and this current has an exponential dependence on the distance between the probe and the surface. A feedback loop keeps this current constant by adjusting the probe-surface distance via a piezoelectric element.

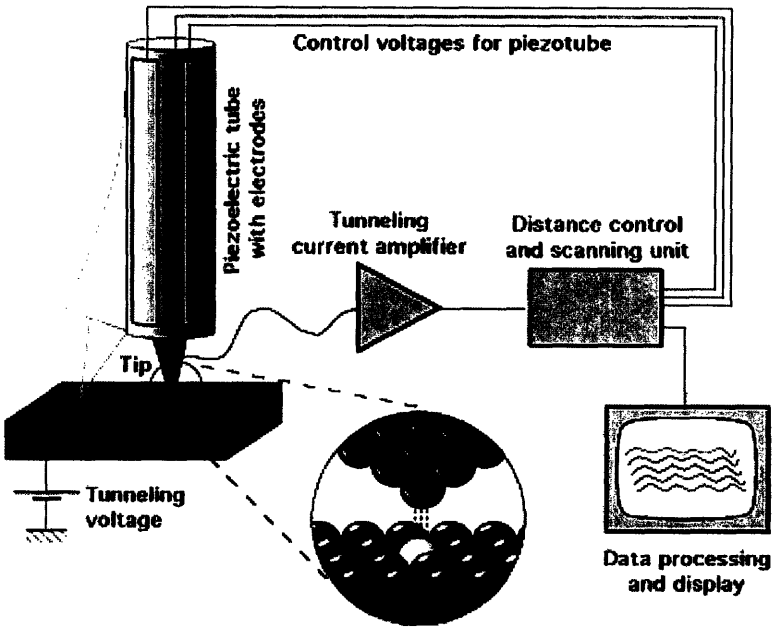

Figure 5. Schematic of STM. Adapted from [37].

When we take a measurement of ripple spacing, it is a measurement of the peak-to-peak distance using the section function in the Nanoscope software. It should be noted that this distance comprises the width of two different domains.

Although we take great care to avoid having external noise in our system, sometimes noise is still present. The way we distinguish between noise and actual features is an important distinction in our research. Several scans are taken at a series of different tip velocities and the ripple spacing is measured. Real features should more or less maintain their spacing with respect to tip speed, whereas noise will scale linearly with tip speed and when the linear fit is extrapolated to zero tip speed the line should go through the origin. We perform this control with all of our nanoparticles to be sure that the features we are observing are real. One example of this analysis is shown in Figure 6.

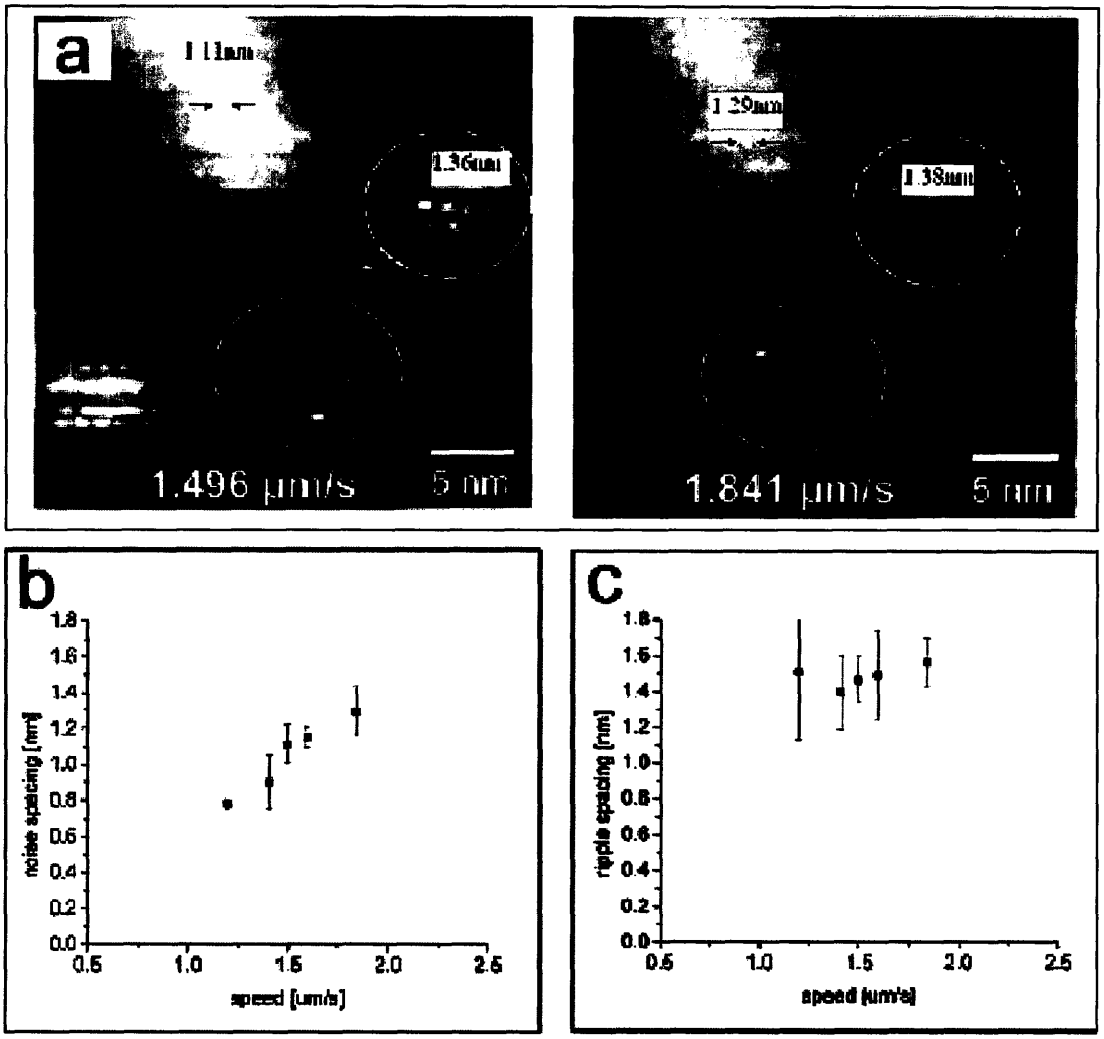

Figure 6: Ripple analysis. (a) STM height image showing two OT:MPA 2:1 nanoparticles, encircled by dotted lines, and their ripple spacing at two different tip speeds. The spacing of the noise on the substrate is also measured at different tip speeds. (b) Noise spacing with respect to tip speed. (c) Ripple spacing with respect to tip speed. Adapted from ref. [33].

Depending on the relation between the scan angle and the orientation of the ripples, the quality of the image can be affected. This phenomenon is related to the fact that the STM forms its images by rastering. If the ripple orientation is not perpendicular to the fast scan direction, the perspective of the scan can at times cause a crosshatched appearance in the ligand shell, making it difficult to discern the actual ripple direction. Another important observation is that when changing the scan angle, the structure and ripple spacing should be expected to change as well, depending on the lattice of the nanoparticles.

The presence of ripples has been found on several ligand mixtures including octanehiol:mercaptoundecanoic acid 1:1, nonanethiol:mercaptohexanol 2:1 and 4-aminothiophenol:hexanethiol 1:1, with average ripple spacings of 0.8-0.9 nm, 0.7 nm, and 0.6-0.8 nm respectively[33] (Figure 7). In all these cases the ligands are significantly different in length and headgroup functionality in order to increase the driving force for

phase separation. Also, note that the thiol end group in all these ligands allow for sufficient mobility and place exchange to ensure that ripple formation can be attained.

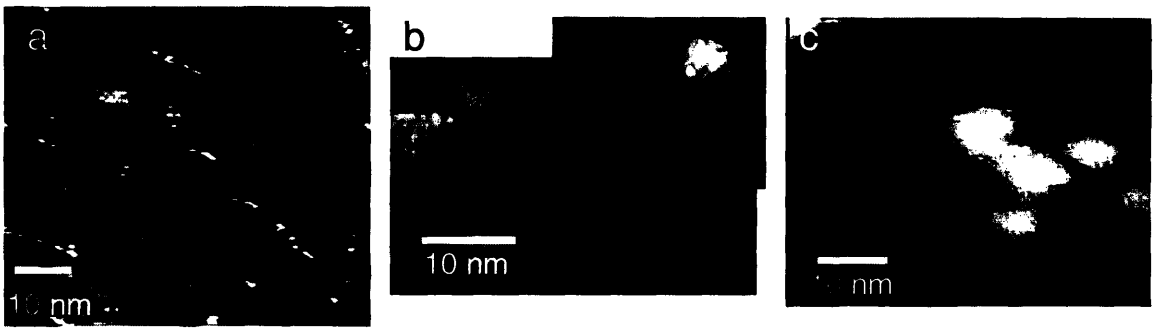

Figure 7: STM height images of rippled nanoparticles of various ligand compositions. (a) Nonanethiol:Mercaptohexanol 2:1 (b) 4-Aminophenylthiol: Hexanethiol 2:1 (c) Octanethiol:Mercaptoundecanoic acid 1:1.

X-ray diffraction (XRD) has also been used to characterize the ripples on the nanoparticles and there were peaks showing periodic arrangements that were never previously observed in homoligand nanoparticles.[34]

The diameter of the core, the chemical nature of the ligands, and the molar ratio of the ligands all play a role in determining ripple spacing. An in-depth analysis of OT:MPA 2:1 nanoparticles showed that ripple spacing was found to increase with respect to nanoparticle core diameter[33] (Figure 8). By varying the molar ratio of the ligands during the synthesis, it is possible to control the stoichiometry of ligands on the nanoparticle itself. Varying these parameters allow different ripple spacings to be achieved.

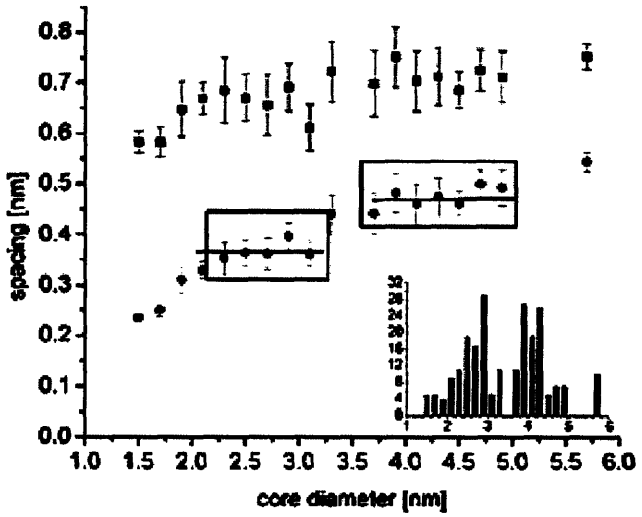

Figure 8. Ripple spacing (black) and sulfur-sulfur spacing (red) with respect to core diameter of OT:MPA 1:1 nanoparticles. Adapted from reference [33].

2.3.2 Properties of rippled nanoparticles

These rippled nanoparticles' unique nanostructure imparts many unexpected properties to these nanoparticles. One surprising characteristic is that the solubility of these nanoparticles depends non-monotonically on ligand shell composition[34] (Figure 9). In other words, solubility behavior cannot be explained based on chemical or composition arguments alone. Furthermore, these nanoparticles have exhibited some demonstrated resistance to non-specific protein adsorption.[34] The alternating hydrophobic and hydrophilic domains prevent proteins from finding a suitable conformation to adsorb onto the nanoparticles. This is not a new idea and forms the functional basis of how dolphin skin, for example, resists biofouling. Other researchers have also used a similar approach, such as Karen Wooley and her work using crosslinked networks of hyperbranched fluoropolymer-polyethylene glycol as anti-fouling coatings.[38]

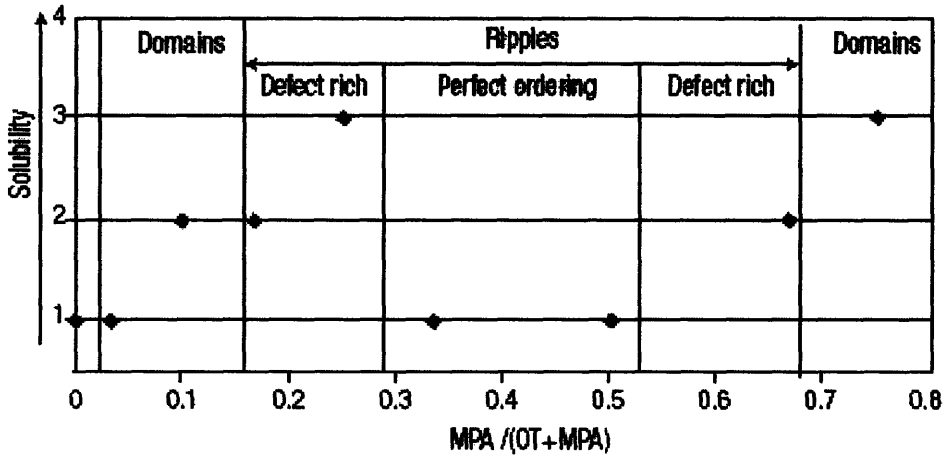

Figure 9. Solubility of OT:MPA nanoparticles in ethanol as a function of MPA fraction. Note the non-monotonic dependence of solubility on the composition of the ligand shell. Adapted from ref [34].

The existence of ripples is also corroborated by recent work by DeVries et al. reporting divalent nanoparticles.[39] This work takes advantage of the fact that on the nanoparticle, the 2D crystal (i.e., the ligand shell) that propagates around the nanoparticle exhibits 2π rotational symmetry, will inevitably form two diametrically opposed defect points at the poles of the nanoparticles. These poles are more reactive than the rest of the nanoparticle surface and have a faster rate of place exchange than the rest of the ligand shell molecules. The phase-separated rings on the rippled nanoparticles even more intensely demarcate the reactive poles. After selectively functionalizing these more reactive poles using place exchange, divalent nanoparticles are formed that can then be used to form chains or self-standing films.

2.4 Background: Water solubility

These previous studies only addressed water-insoluble nanoparticles.[33,34] Alkanethiolate MPMCs are hydrophobic and cannot be dispersed in an aqueous

environment, but in order to use these nanoparticles in biological systems, they must be water-soluble. Researchers have come up with a multitude of approaches for solubilizing gold nanoparticles in water, including using charged ligands,[1,40] ligands terminated with ethylene glycol moieties,[41] various macromolecules,[11,42-46] and others.[47]

When a macromolecule is used to make a nanoparticle hydrophilic, one would not necessarily expect the macromolecules to form a SAM. Their large size provides them with too much conformational freedom to form an ordered monolayer on a flat surface.[48] In other words, there is a negligible enthalpic contribution to mixing in these cases, so we expect perfect mixing behavior when there are two components or more. It follows that these types of systems would not form an ordered monolayer on a curved surface either.

On the other hand, charged thiolated molecules can indeed form ordered SAMs on flat gold due to stabilizing Van der Waals forces between the molecules,[48] and thus it is possible that they could form 3-D SAMs on gold nanoparticles and possibly phase separate into ordered domains.

3 Sulfonated gold nanoparticles

We have chosen to put a sulfonate group on these nanoparticles because it is always charged in the range of physiological pH, and it is one of the strongest anions in the Hofmeister series. The Hofmeister series is often described as how capable an ion is of stabilizing a protein, but it can more generally be described as the phenomenon of ions having different properties at the same ionic strength.[49] Solubilities depend not just on the charge of the ion, but its nature. Sulfates are strongly hydrated and will interact with the hydration layer of proteins in a way that makes the surrounding buffer a poorer solvent.[50]

The 11-carbon backbone was a direct result of the MUS synthesis, as shown in Figure 10. We also wanted the hydrophilic ligand to be longer than our 8-carbon hydrophobic ligand (OT) to maximize the water solubility of the nanoparticles.

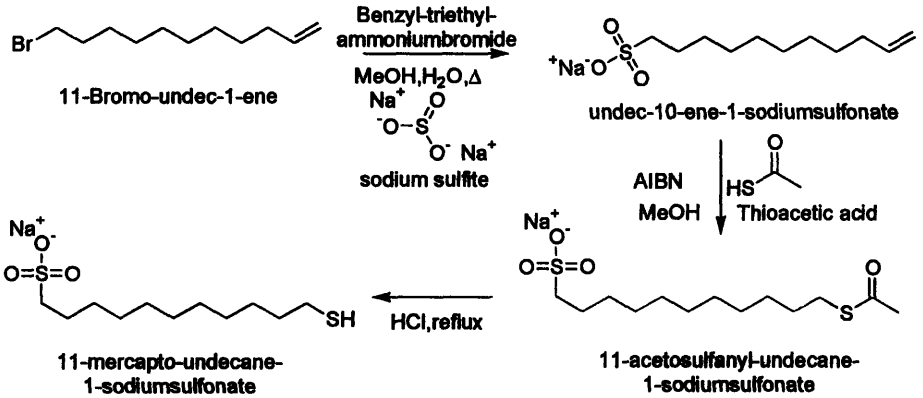

Figure 10. Synthesis of mercapto-undecane-1-sodiumsulfonate, also known as mercaptoundecanoic acid.

The resulting sulfonated nanoparticles are extremely water soluble even at a relatively low fraction of mercaptoundecasulfonic acid. Their negative charge and their extreme hydrophilicity were properties that were specifically engineered, but these

properties also present new challenges for sample preparation and characterization. We normally use solvents such as toluene to prepare nanoparticle samples, but we must deal with water when handling these nanoparticles. The formation of dense nanoparticle layers aids imaging due to increased stability and resistance to motion, but the net charge on these sulfonated nanoparticles prevents them from forming these kinds of layers, and they are prone to movement during imaging. We also suspect that there may be residual water on the nanoparticles which would also make imaging difficult. In the following sections I will present paths to overcoming these issues.

Preliminary results have shown that nanoparticles protected with a ligand shell containing sulfonate groups interact with human cells in interesting ways. Our hypothesis is that the behavior of these nanoparticles is in part due to the unique morphology of the ligand shell and I will attempt to correlate this with my STM data. To this end I have been engaging in a systematic study to determine the morphology of the ligand shell of these nanoparticles.

4 Experimental

4.1 Nanoparticle Synthesis

All materials were purchased from Sigma Aldrich and used as received. A one-phase nanoparticle synthesis method was used.[14] 200 mL abs. ethanol (EtOH) was stirred in a 500 mL round bottom flask on an ice bath for 10 min. 0.9 mM HAuCl4•H2O (355 mg) was dissolved in EtOH, and after 10 min 0.9 mM of thiol was added to the reaction mixture. The relative ratios of different thiols varied depending on the desired ligand shell composition, but the total amount of 0.9 mM remained constant. After stirring the reaction mixture for another 10 min, 200 ml of a supersaturated solution of NaBH4 in ethanol was added all at once, causing the solution to turn black. The solution was then stirred for another 3 h and refrigerated overnight to precipitate. The supernatant solution was removed, and the remaining solution containing the nanoparticles (~5 ml) was filtered through quantitative filter paper. After filtration, the nanoparticles were rinsed with 200 mL ethanol followed by 200 mL methanol, and then dried thoroughly under air. The advantage over a two-phase synthesis is that no phase-transfer agent (i.e. (TOA)Br), which is generally difficult to fully remove from the ligand shell, is required. A schematic of the resulting nanoparticle is shown in Figure 11.

Throughout this paper we assume that the stoichiometric ratio used in the reaction is also the ratio found on the particles' ligand shell. This concept has been confirmed for OT:MPA nanoparticles using FTIR,[51] and further study to confirm this assumption in this particular system is underway.

The synthesis resulted in nanoparticles polydisperse in size, with core diameters ranging from ~2-10nm, as determined by TEM and confirmed with STM.

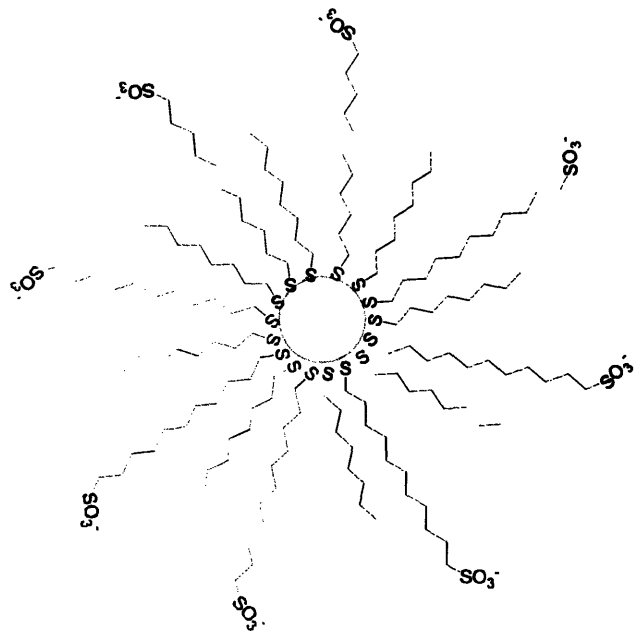

Figure 11. Schematic of MUS:OT nanoparticle.

4.2 Sample Preparation

4.2.1 Nanoparticle solution

1 mg of MUS:OT 1:2, MUS:OT 1:1, MUS:OT 2:1, All-MUS, or MUS:branched OT 1:2 nanoparticles are dissolved in 1 ml of DI H_20. Some samples require sonication for 20 minutes before filtering with a 0.2 μM PTFE syringe filter (Nalgene, Rochester NY). Subsequent sample preparation methods use this nanoparticle solution.

4.2.2 Dropcasting at room temperature

A drop of nanoparticle solution is placed on bare Au (111) on freshly cleaved mica (Molecular Imaging) and the solution is covered and allowed to evaporate at room temperature.

4.2.3 Casting on a heated substrate

A piece of bare Au (111) on freshly cleaved mica (Molecular Imaging) is placed on a metal puck using carbon tape, and this substrate is placed on a hotplate at about 120°C. After waiting ~5 minutes for the substrate to heat up, ~2 μL of this nanoparticle solution is cast onto the substrate. The volume of nanoparticle solution used will depend on the size of the piece of gold on mica. The heat causes the water to bubble and evaporate quickly (within 2-3 s), effectively "freezing" the solution distribution of nanoparticles onto the substrate.

4.2.4 Soaking substrate in nanoparticle solution

Bare gold on mica was soaked in nanoparticle solution for several (~3) days. After incubation the gold is rinsed with ethanol and allowed to air dry.

4.2.5 Water + hexamethonium chloride nanoparticle solution

1 mM and 10 mM Hexamethonium chloride $(CH_3)_3N(Cl)(CH_2)_6N(Cl)(CH_3)_3$, Sigma Aldrich) was added to the nanoparticle solution. The positive charges should serve almost as a dithiol to crosslink the nanoparticles to each and other and to the surface of the gold as well.

4.2.6 Water + methanol nanoparticle solution

Some samples have been prepared with 1 mg of nanoparticles in 1 ml of DI H_20 plus 1 ml of methanol. The more dilute sample plus the added methanol were advantageous in creating a dispersed sample when casting on a heated substrate.

4.2.7 Monolayer formation

For formation of an MUS monolayer, 1 mg of MUS was dissolved in 1 ml of methanol. This mixture was sonicated for 20 minutes. Bare Au on mica was immersed in this solution for several days (~3). The substrate is then rinsed thoroughly with fresh methanol. Formation of the MUS:OT 1:2, OT, MUS:OT 1:10, and MUS:OT 1:5 monolayers were formed similarly, only with varying ratios of MUS and OT in methanol.

4.3 Imaging

STM images were obtained using a Digital Instruments Multimode Nanoscope IIIa equipped with an E scanner. Pt/Ir tips were purchased from Veeco and used new or mechanically cut. Typically a bias voltage of -1.2 to -1.4 V, a set current value of ~600 pA, and a tip speed of 0.3-1.3 um/s were used. Integral gains and proportional gains had typical values of ~0.6 and ~0.8-2.0, respectively.

A low-current STM head was also used for some of the studies. Typical bias voltages of 1-1.2V, a set current value of ~25-50 pA, and a tip speed of 0.3-0.5 μm/s were used. Integral gains and proportional gains had typical values of ~0.6 and ~0.8, respectively.

5 Results and Discussion

5.1 Stability

All nanoparticles used in this study are stable for several weeks if not months in solution. They begin to crash out of solution if more than approximately a 1:1 ratio of ethanol or methanol is added. At salt concentrations of 250 mM some nanoparticles precipitate out of solution, and at 500 mM most nanoparticles are insoluble.

5.2 Sample Preparation

Although we understand the behavior of the ligand shell of hydrophobic mixed monolayer nanoparticles quite well, nanoparticles with a sulfonated ligand are quite different. Standard nanoparticle STM sample preparation techniques were optimized for nanoparticles dissolved in organic solvents[33]. The basic procedure is to expose an

alkanedithiol monolayer-covered gold substrate to a nanoparticle solution that usually also contains dithiols[52] (Figure 12). The nanoparticles form a well-packed monolayer as shown in Figure 13a that is relatively easy to image.

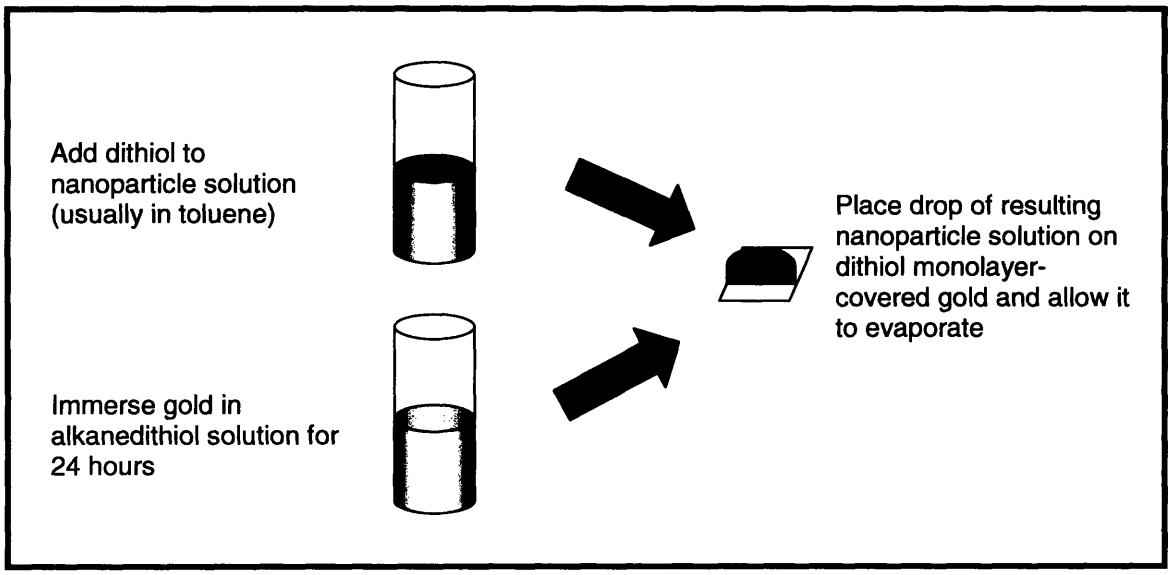

Figure 12. Schematic illustrating standard sample preparation method.

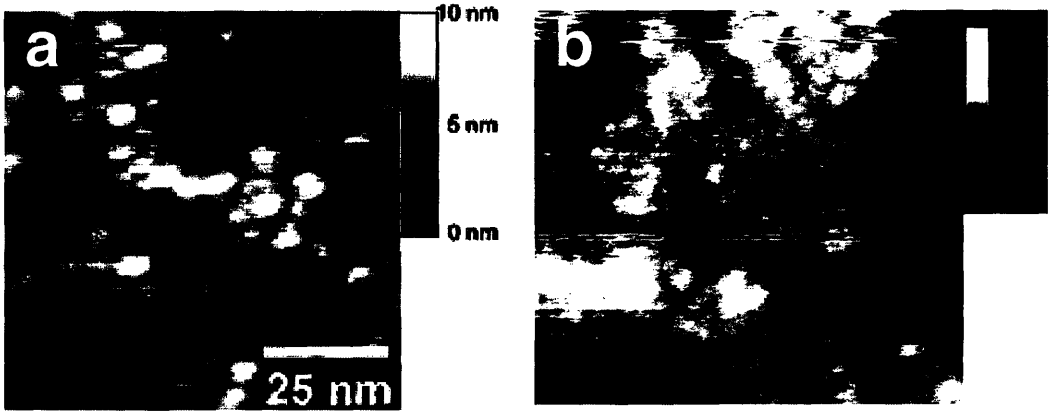

Figure 13. (a) STM height image of OT:MPA 2:1 nanoparticles prepared using the standard sample preparation method, displaying hexagonal packing. Adapted from ref [33]. (b) STM height image of MUS:OT 1:1 nanoparticles prepared using the standard sample preparation method, displaying large aggregates.

However, these sulfonated nanoparticles are different from the alkanethiolate nanoparticles as they can only be dissolved in water and they always carry a negative charge. Nevertheless, we used the standard procedure as a starting point for the sample preparation of these water soluble particles. Unfortunately, we found that few particles, if any, were transferred to the substrate. In addition, the nanoparticles were not directly attached to nor were they interdigited in the dithiol monolayer, which is likely due to the hydrophobic nature of the alkanedithiol SAM as opposed to the hydrophilic nature of the nanoparticles. Thus the nanoparticles were not immobilized on the surface at all.

Furthermore, the effective tunneling barrier from the gold substrate to the particle core was extremely large, requiring high voltages that could drive particles away from the tip and make imaging nearly impossible.

Another difficulty was that we were not able to crosslink the nanoparticles together using dithiol because it was difficult to solubilize the dithiol molecules in the aqueous solution of nanoparticles, a technique we commonly used when imaging non-hydrophilic nanoparticles[33]. Furthermore, even if the dithiol were water-soluble that does not necessarily mean they would be able to penetrate the ligand shell of these sulfonated nanoparticles.

Our standard sample preparation method consisted of placing a drop of nanoparticle solution onto the gold substrate and allowing the solvent to evaporate under ambient conditions. However, large aggregates of the nanoparticles formed that made the samples difficult to image, as shown in Figure 13b. It is not likely that molecular resolution would be achieved if there are multilayers of nanoparticles, because the layers would form an insulating barrier to the tunneling of electrons. The relatively slow evaporation of water as compared with other solvents was suspected to be exacerbating the clumping. To mitigate this effect, I tried casting the aqueous nanoparticle solution on a heated substrate (Figure 14) to accelerate the evaporation of water, both minimizing the agglomeration effects and allowing for the formation of regions of disperse monolayers of these nanoparticles. Furthermore, the heat removes excess water that may have remained in the ligand shell in samples prepared entirely at room temperature. In this manner we were able to achieve the first STM images of these nanoparticles.

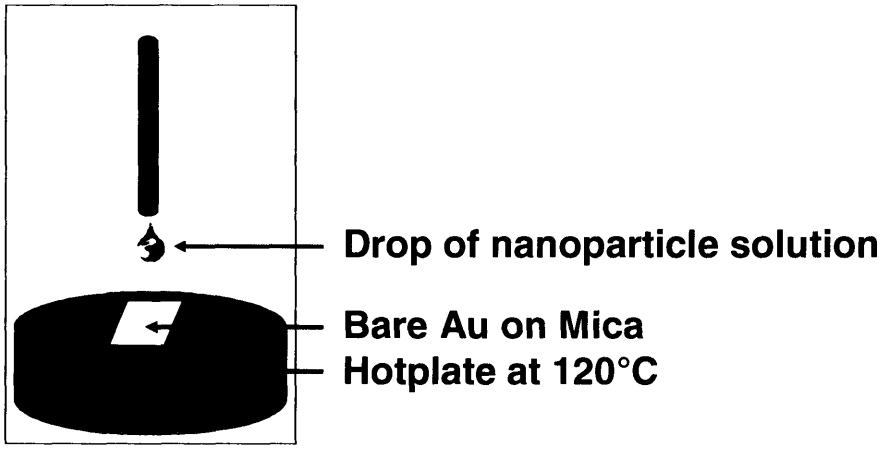

Figure 14. Schematic showing new sample preparation method.

More recently, samples have been prepared with 1 mg of nanoparticles in 1 ml of DI H_20 plus 1 ml of methanol. The more dilute sample was advantageous in creating a dispersed monolayer. The methanol serves two purposes: it lowers the surface energy of the water, distributing the nanoparticle solution more evenly and quickly over the gold (instead of creating a droplet as occurs with pure water); it also has a lower boiling point. Both these effects lead to the solution evaporating faster, which more effectively freezes the nanoparticles to the surface.

5.3 Sample Preparation Variations

It is clear that a more consistent and reproducible sample preparation method is needed. Many approaches were taken, as summarized in Table 1. It is clear that dropcasting on a heated substrate, as described in section 4.2.3, has proved to be the most effective sample preparation method for these sulfonated nanoparticles.

I tried to make a monolayer of nanoparticles by adding ethanol to the water and nanoparticle solution. In theory, this would cause the nanoparticles to have more affinity for the gold than for the solvent. The gold substrate was placed at a 45° angle. The sample was then placed in the oven at 50°C until the nanoparticle solution evaporated. As the solution evaporated, it was hoped that it would deposit nanoparticles on the liquid-air boundary, eventually coating the entire substrate as the evaporation front moves downward. Unfortunately, the nanoparticles were unevenly distributed on the gold and did not form an imageable monolayer. However, the inadvertent formation of thiol SAMs on my gold substrate occurred often (Figure 15). I believe that this was due to free thiols in solution that were originally interdigitated in the ligand shell, or that came off the nanoparticle itself. I have also seen the presence of what appear to be phase-separated domains. The heat from the oven apparently provided a stronger driving force than just soaking them at room temperature. I often observe etch pits on our gold, even when I did not previously create a SAM on the gold. I believe that these etch pits are due to thiols leaving the nanoparticle surface and adsorbing onto the gold, and a rough calculation confirmed the possibility of this happening as only an estimated 1-2 ligands per nanoparticle would have to leave the ligand shell to create a full SAM on the gold substrate.

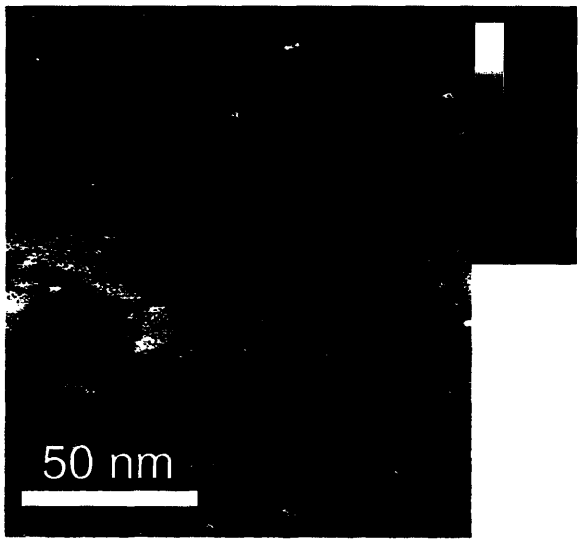

Figure 15. STM height image showing an attempt at sample preparation using ethanol and water and evaporating on an angled bare Au(111) substrate. No nanoparticles are clearly observed. Note the presence of etch pits despite there being no preformed SAM.

I also tried creating a positively charged monolayer on the gold surface[53,54] to electrostatically attract particles to the surface. I attempted to form a cysteamine ($HSCH_2CH_2NH_2$) SAM on the gold on mica from either water or ethanol, each at concentrations of 100uM, 1mM and 10mM. Unfortunately, STM characterization of

these surfaces showed the tendency of the molecule to form three-dimensional aggregates on these surfaces, as shown in Figure 16. Having an atomically flat substrate is essential for STM, so I eliminated cysteamine-covered gold on mica as a candidate for sample preparation.

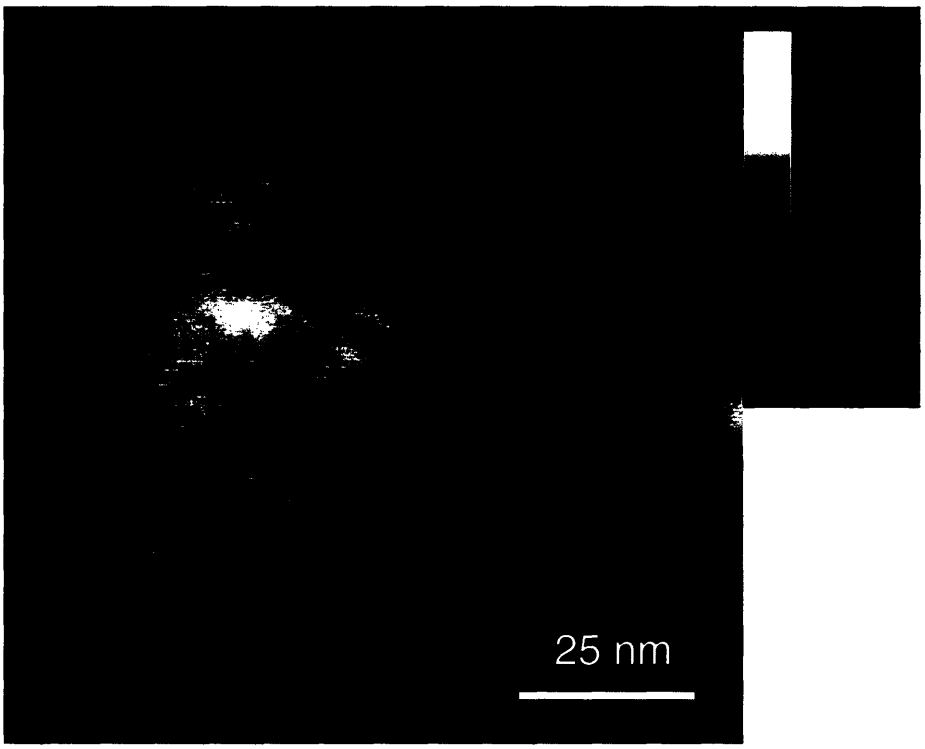

Figure 16. STM height image of Au(111) on mica soaked in 10mM cysteamine hydrochloride solution overnight.

One of the probable factors preventing the nanoparticles from packing nicely is their surface charge. Increasing the ionic strength of the solvent could theoretically screen charges more effectively. About 1 mg of nanoparticles was placed in solutions of varying concentrations: 10mM, 100mM, 250mM, and 500mM NaCl in MilliQ water, which correspond to ionic strengths of 0.01, 0.1, .25, and 0.5 respectively. They were then cast using three different methods: soaking the gold in the solution, dropcasting at room temperature, and dropcasting on a heated substrate. The nanoparticles are not soluble in 500mM NaCl water and are only partially soluble in 250 mM NaCl water. None of these samples exhibited any improvement in the sample preparation; the nanoparticles continue to aggregate and do not form well-packed monolayers.

I have also tried to make a film of these nanoparticles to aid in the imaging process. It is our hope that once they are in a film, the nanoparticles will stabilize each other and prevent each other from moving during imaging. I tried to make a pseudo-Langmuir-Blodgett film by adding a solvent that is heavier and has a higher boiling point than water to the nanoparticle and water solution. These constraints only allow a limited number of solvents left to choose from, of which dichlorobenzene is one. However,

when I evaporated off the water, the nanoparticles segregated to the edges of the vial, forming a ring. The dichlorobenzene did not want to wet the surface of the water.

One of the concerns in using a dithiol monolayer as we do in our standard sample preparation method for hydrophobic nanoparticles is that the dithiol monolayer is very hydrophobic. It is unlikely that our hydrophilic nanoparticles would want to interact with this monolayer. I thus tried to use a dithiol that has an ethylene glycol-like backbone: 3,6-dioxa-1,8-octanedithiol ($C_6H_{14}O_2S_2$, hereafter referred to as DODT) to form a monolayer on gold (Figure 17). Dropcasting nanoparticles at room temperature yielded large aggregates, and soaking the nanoparticles did not work well either. When nanoparticle solution was dropped onto a heated substrate, however, the nanoparticles formed well-defined packed aggregates, as shown in Figure 18. It is strange that a monolayer of DODT would cause the nanoparticles to cluster and pack this way. It is possible that there are DODT molecules leaving the gold substrate, entering the nanoparticle solution, and cross-linking the nanoparticles by place-exchanging with the nanoparticles' original ligands. I also attempted to add DODT to nanoparticle solution to cross-link the nanoparticles, but this had little to no effect.

Figure 17. STM height image of Au(111) on mica soaked in 10mM ethanolic solution of 3,6-dioxa-1,8-octanedithiol overnight.

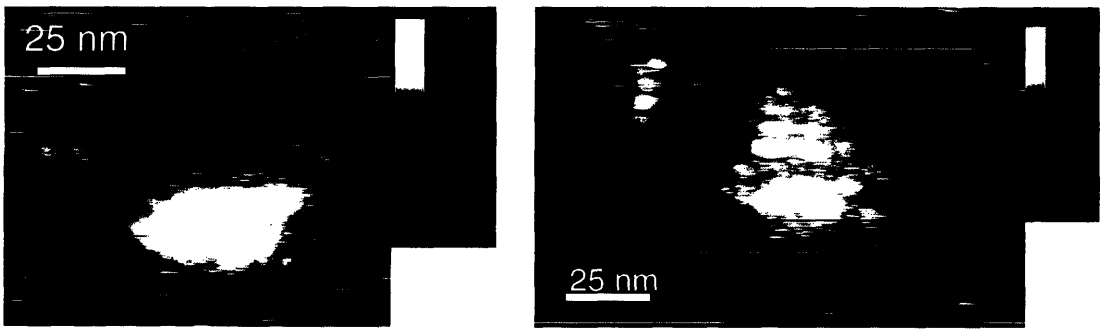

Figure 18. STM height image of MUS:OT 1:2 nanoparticles dropcast on a heated substrate consisting of a 3,6-dioxa-1,8-octanedithiol monolayer on Au(111) on mica.

Hexamethonium chloride has two positive charges and we expect that its dual charges will crosslink the negatively-charged nanoparticles, as well as interact with the gold and perhaps anchor the nanoparticles to the gold as well. At molar concentrations of 1 mM and 10 mM in water, bare gold soaked in hexamethonium chloride formed small 2-3 nm aggregates that could resemble nanoparticles. This was obviously problematic for my studies. However, relatively large particles were found in the images that seemed anchored to the surface during imaging. I made sure to disregard features in my images that resembled the aggregates shown in Figure 19.

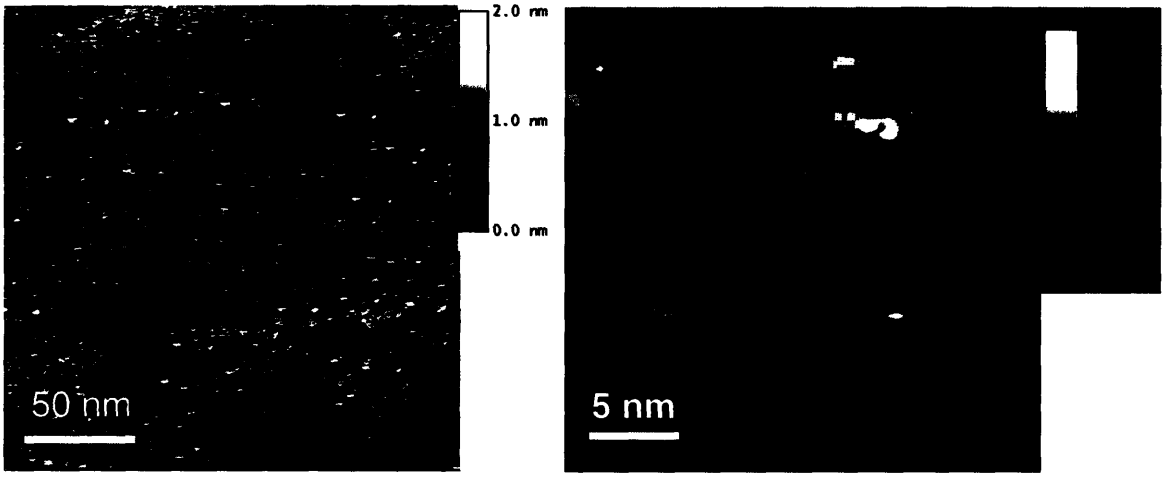

Figure 19. STM height image showing bare Au(111) soaked in 10 mM hexamethnoium chloride. Note that there are no nanoparticles present, but there are aggregates of the molecule that could resemble nanoparticles.

The majority of the following nanoparticle images were obtained by dropcasting a solution of nanoparticle and water or a solution of nanoparticle, water, and methanol onto a heated substrate, but at times one of the variations of the techniques described above was used. These cases will be clearly indicated in the figure captions.

Table 1. Chart summarizing various techniques that were tried. Red signifies techniques that did not work, yellow signifies techniques that worked for some ligand ratios, and green signifies techniques that worked. DODT stands for 3,6-dioxa-1,8-octanedithiol.

	Sample Preparation Method		
Substrate/Solution	Dropcast at RT	Dropcast at 120°C (hotplate)	Soaked
Bare Au	●	●	
Cysteamine hydrochloride* monolayer	●	●	●
Various alkanedithiols	●	●	●
DODT† monolayer	●	●	
DODT in nanoparticle solution	●	●	
H2O:Methanol 1:1 solution	●	●	●
Varying salt concentrations	●	●	●
Hexamethonium chloride in nanoparticle solution	●	●	

5.3.1 All-MUS nanoparticles

The all-MUS nanoparticles, whose TEM data is shown in Figure 20, appear not to have defined structure on their surface. I wanted to image these as a control; if there seemed to be ripples or domains in the ligand shell I would know that my methods were

faulty. The images obtained (3 different samples and approximately 30 images) do not exhibit any

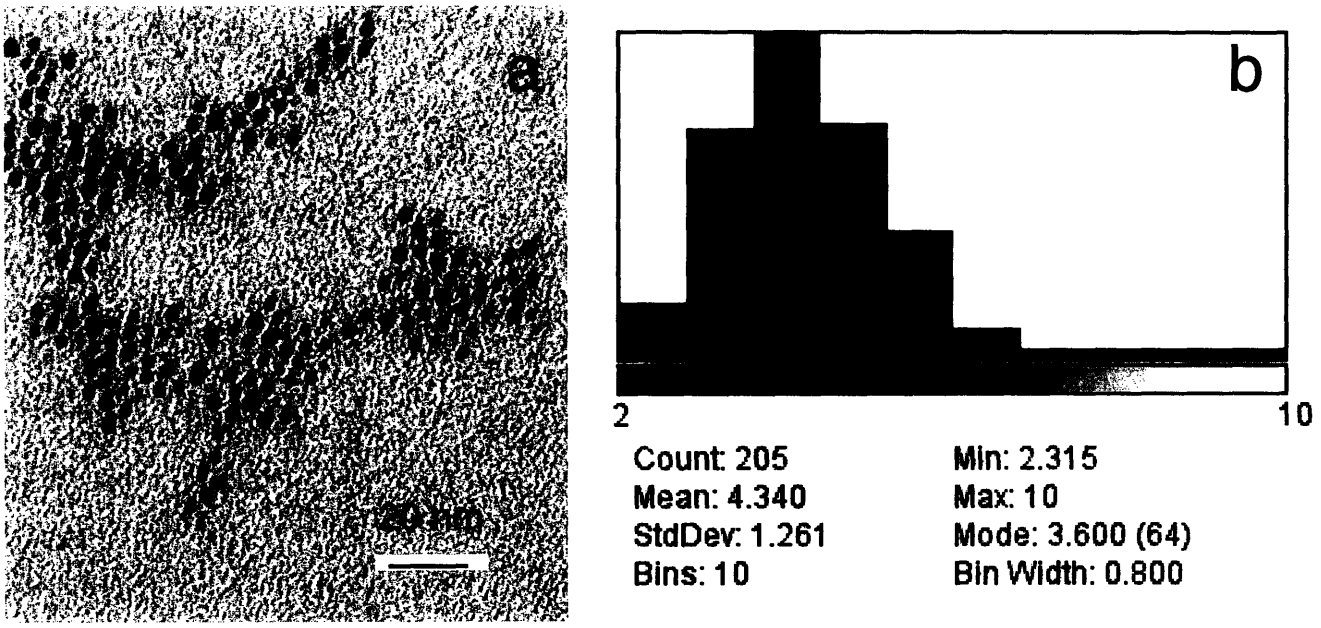

Figure 20. (a) TEM micrograph of all-MUS nanoparticles (b) Size distribution analysis on all-MUS particles. Average particle diameter is 4.34 ± 1.26 nm, with 205 particles counted

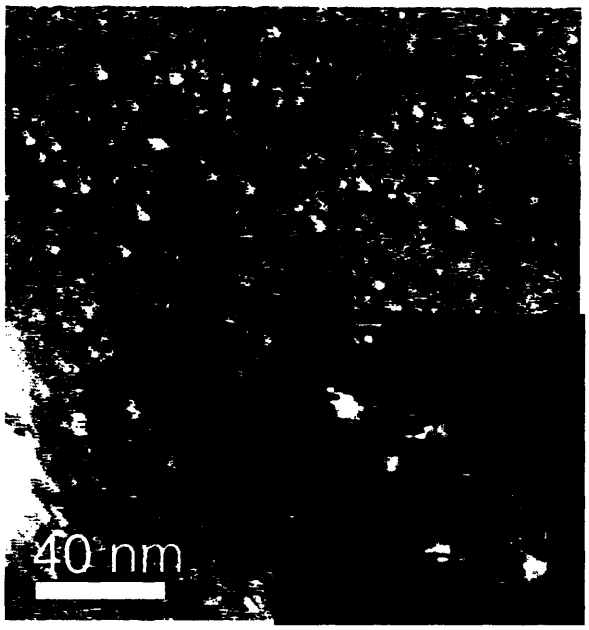

Figure 21. STM height image of all-MUS nanoparticles, cast on heated Au(111) substrate.

5.3.2 MUS:OT 1:1 nanoparticles

The STM images are in agreement with the TEM data, which showed a polydisperse nanoparticle population of about 2 nm to 10 nm in size. Ripples were observed in approximately 75% of the nanoparticles (Figure 22). A section is shown in Figure 23.

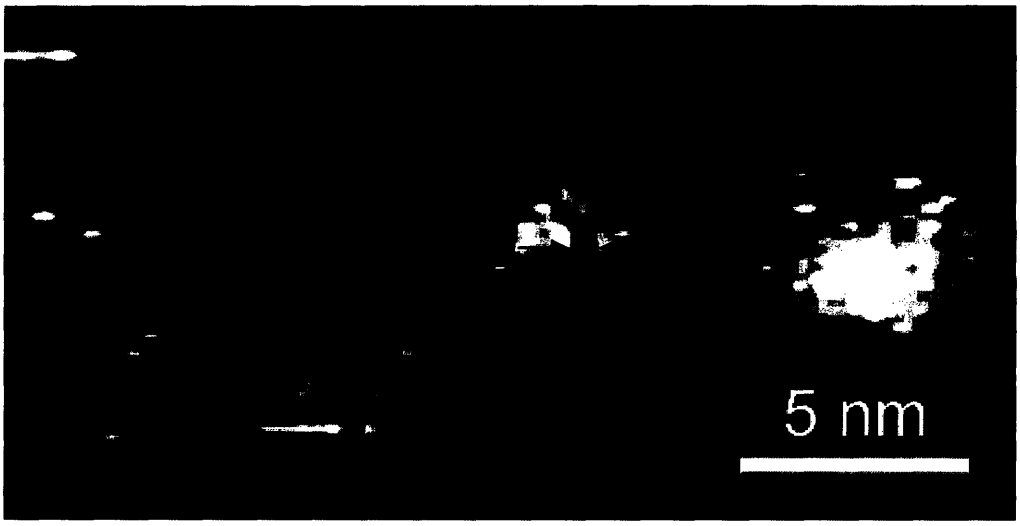

Figure 22. STM height image of MUS:OT 1:1 nanoparticles cast on bare Au(111) on mica, circled with the dotted lines. Ripple spacing is shown between the two red arrows.

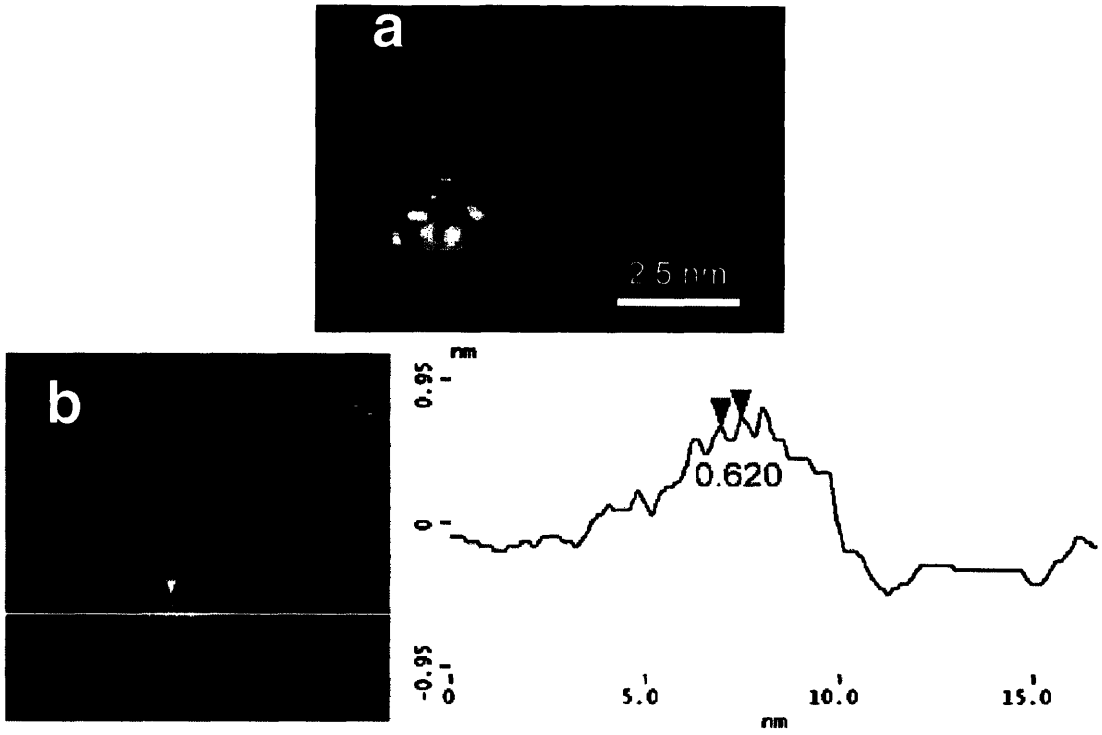

Figure 23. (a) STM height image of MUS:OT 1:1 nanoparticles cast on bare Au(111) on mica, encircled with the dotted lines. Note that their ripples are of different orientations (b) Same nanoparticles as in (a), showing a section measurement between two ripples, with a peak-to-peak spacing of 0.620 nm.

The ripple spacing data consists of two regimes, segregated according to sample size. One set of data was taken from nanoparticles in the size range of 7-10 nm in diameter, and the other was taken from nanoparticles in the size range of 3-5 nm in diameter (

Figure 24). This result correlates with previous findings that ripple spacing increases with increasing diameter of nanoparticles.[33] It generally seems that when casting, nanoparticles of similar size will end up in a similar area on the substrate. During one imaging session (described as one engage-disengage cycle) the nanoparticles will all approximately lie in the same size range. Once these two data sets are disambiguated it is clear that the data is not simply due to noise.

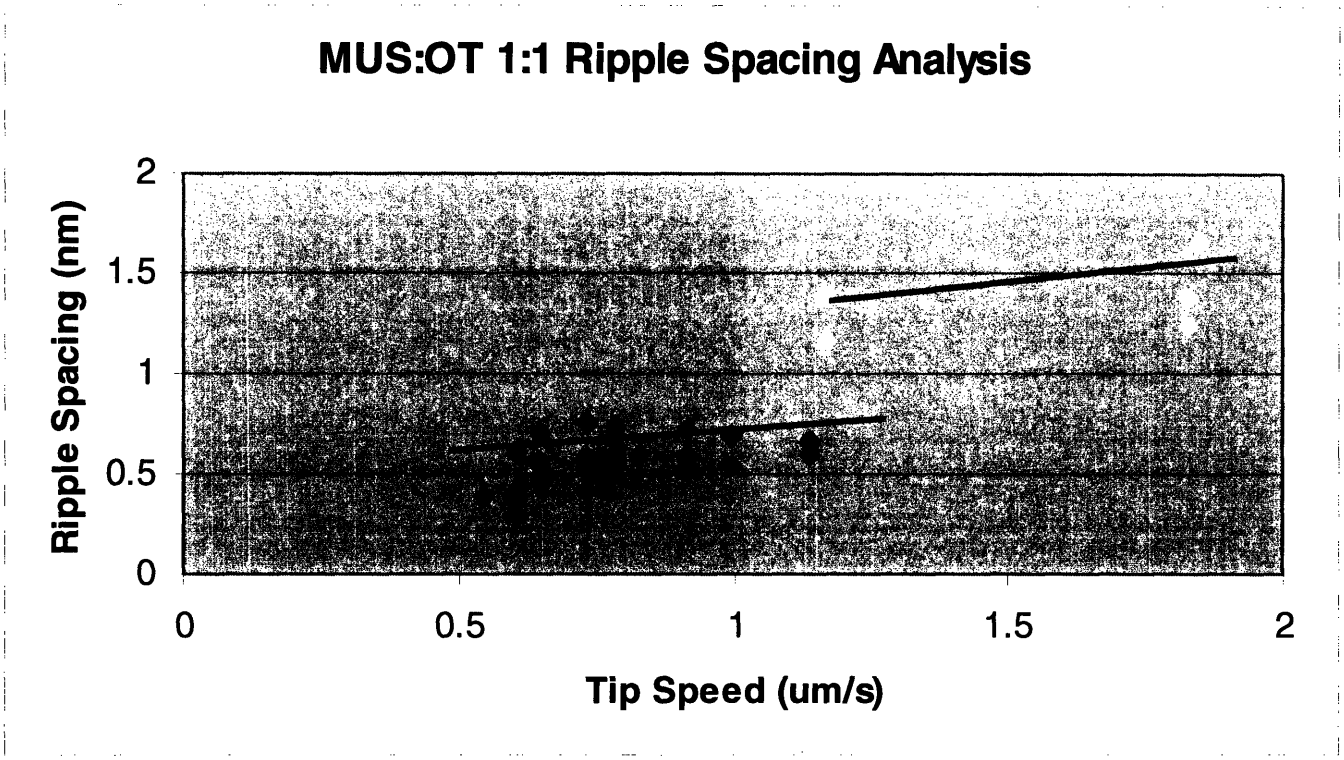

Figure 24. Ripple spacing versus tip velocity for full polydisperse population of MUS:OT 1:1 nanoparticles. Red lines have been drawn only to guide the eye. They show two regimes of data, the smaller ripple spacing data (in blue) corresponding to nanoparticles between ~3-5 nm in diameter, the larger ripple spacing data (in yellow) corresponding to nanoparticles between ~7-10 nm in diameter.

The plot of ripple spacing shown in Figure 25 is only weakly dependent on tip velocity, and thus we believe that the ripple features on these nanoparticles are real. The slight slope could be due to convolution with noise, measurement error or a combination of the two.

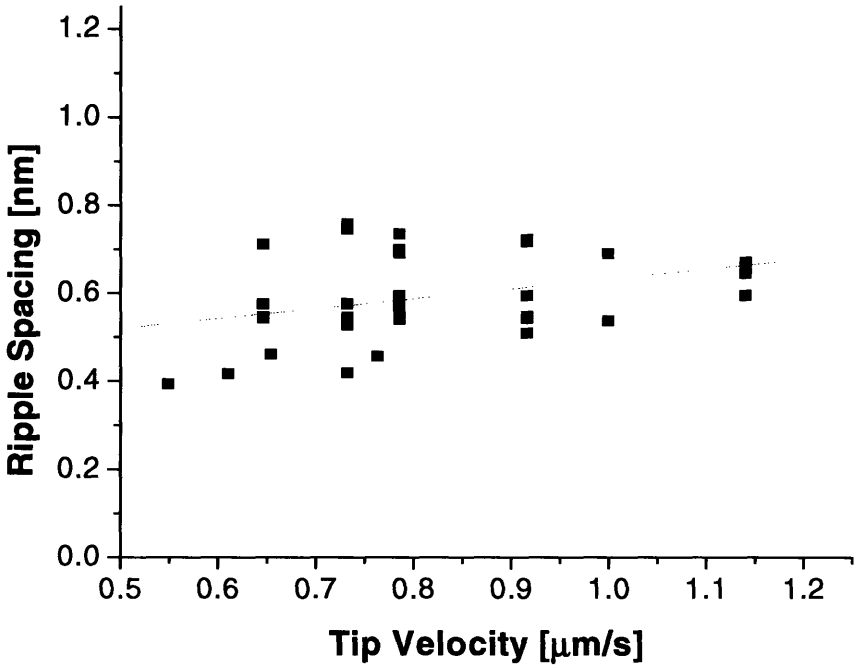

Figure 25. Plot of ripple spacing of MUS:OT 1:1 nanoparticles of diameters between ~3-5 nm with respect to tip velocity during imaging. The red line is a linear fit to the data, with the equation y = 0.406 + 0.228x. Average ripple spacing is 0.59 nm.

5.3.3 MUS:OT 2:1 nanoparticles

MUS:OT 2:1 nanoparticles have a similar size distribution as the other nanoparticles so far (Figure 26). I have obtained some images of MUS:OT 2:1 nanoparticles (Figure 27, Figure 28), but often the ligand shell looks streaky even if the nanoparticle itself does not appear to be moving around. It is possible that the increased hydrophilic component in these nanoparticles renders them more difficult to image. Some of the nanoparticles seem to have holes in their ligand shell, which I will discuss in more detail later in section 5.3.5.

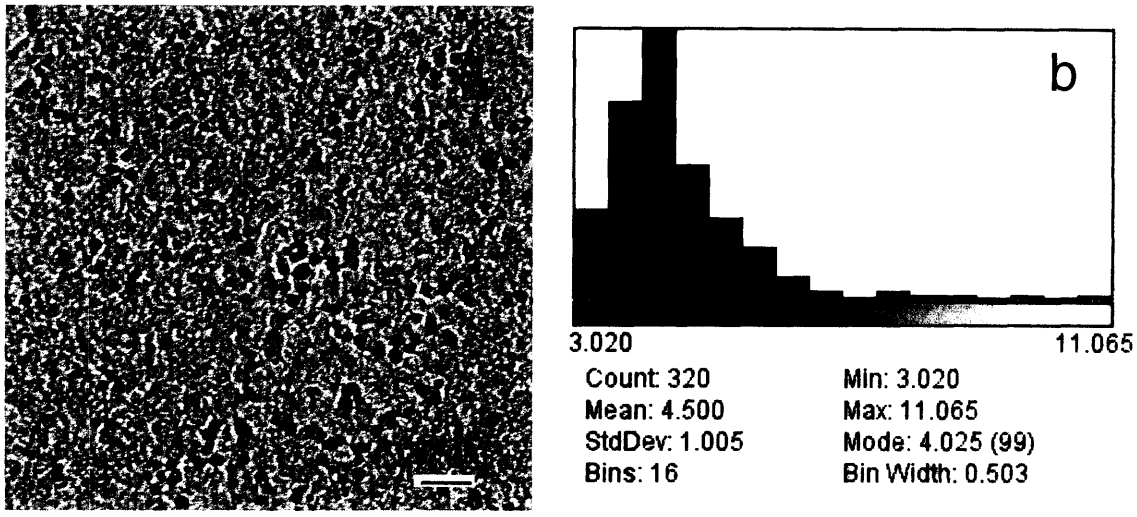

Figure 26. (a) TEM micrograph of MUS:OT 2:1 nanoparticles (b) Size distribution analysis of MUS:OT 2:1 nanoparticles. Average particle diameter is 4.50 ± 1.00 nm, with 320 particles counted

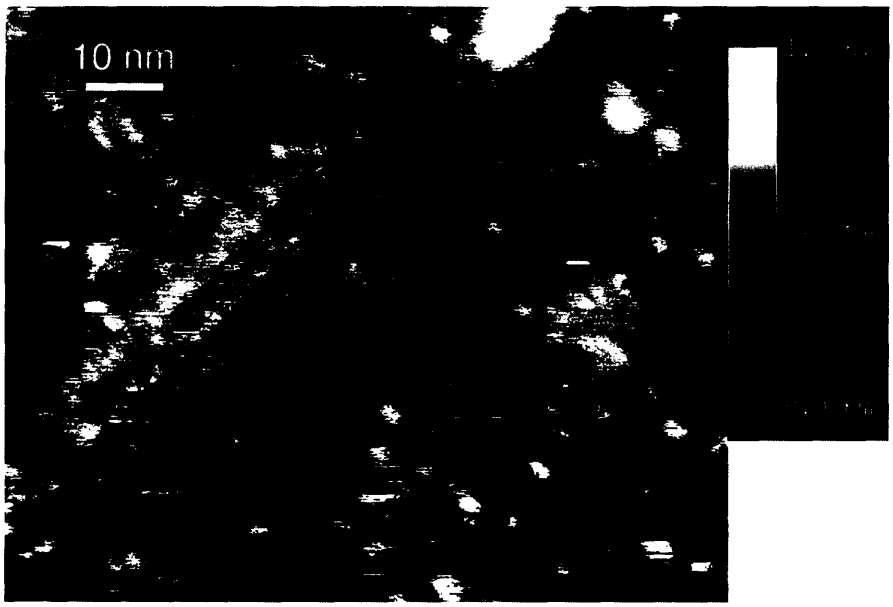

Figure 27. STM height image of MUS:OT 2:1 nanoparticles on Au (111) on mica. Sample was prepared with 1mM hexamethonium chloride, dropcast on a heated substrate.

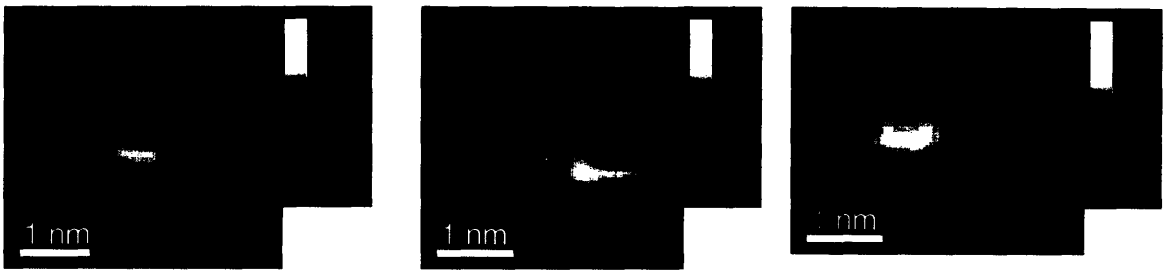

Figure 28. Zoomed-in STM height images of single MUS:OT 2:1 nanoparticles on Au (111) on mica. Samples were prepared with 1mM hexamethonium chloride, dropcast on a heated substrate.

5.3.4 MUS OT 1:2 nanoparticles

TEM of MUS:OT 1:2 nanoparticles are shown in Figure 29. The images I have acquired of MUS:OT 1:2 nanoparticles are puzzling (Figure 30). They do not all seem to be rippled, but they do seem to exhibit some structure on the surface. If there are ripples present I only see them in a very few number of nanoparticles per scan (perhaps 5% or so), in contrast with the MUS:OT 1:1 nanoparticles, where approximately 60-70% of the nanoparticles in each scan would exhibit visible ripples (Note that even if 100% of the nanoparticles were rippled, one would only expect a fraction of these ripples to be visible with the STM due to variations in orientation, etc.). A larger portion of the nanoparticles exhibit some random phase-separation that is not manifested as rings around the nanoparticle surface, as in rippled nanoparticles, but as disorganized domains. Often, hole formation can observed.

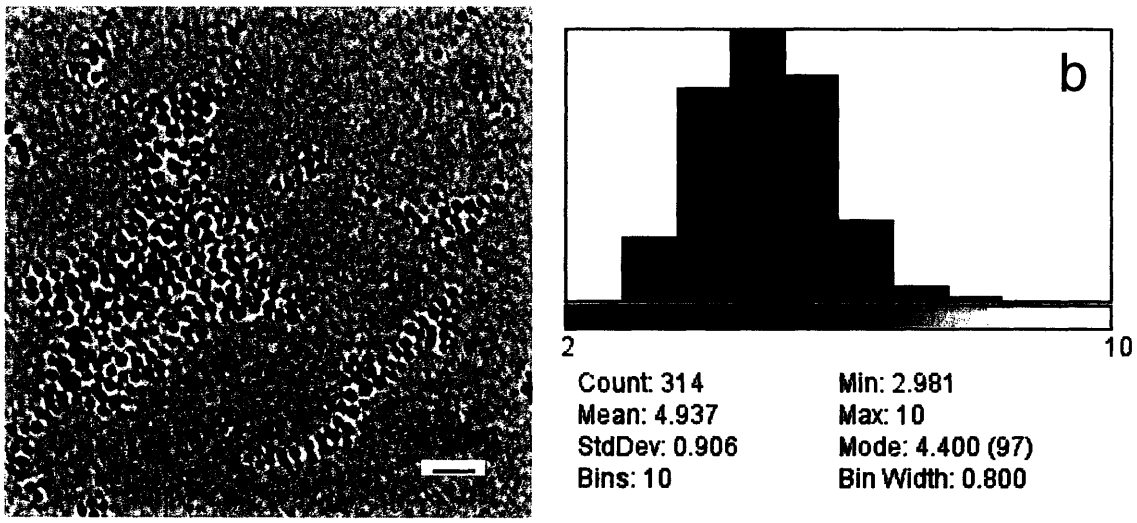

Figure 29. (a) TEM micrograph of MUS:OT 1:2 nanoparticles (b) Size distribution analysis of MUS:OT 1:2 nanoparticles. Average particle diameter is 4.93 ± 0.906 nm, with 314 particles counted

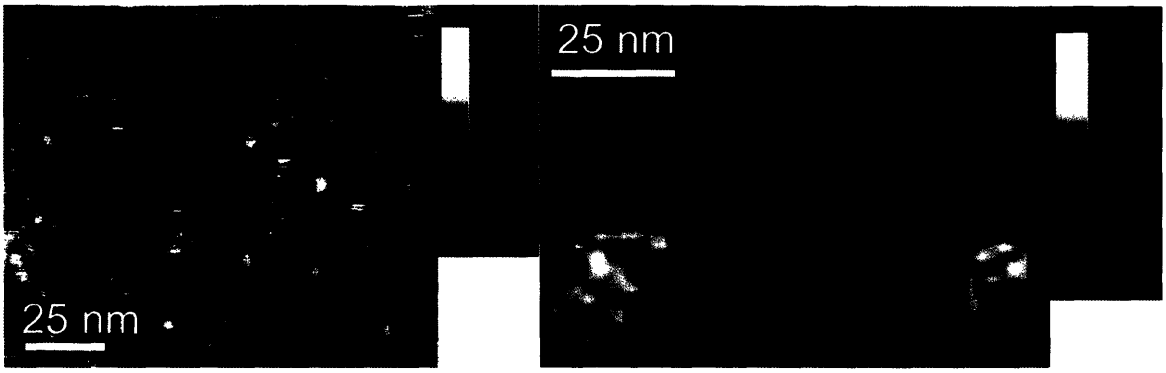

Figure 30. STM height images of MUS:OT 1:2 nanoparticles in water and 1mM hexamethonium chloride. Dropcast on a heated substrate.

5.3.5 MUS:branched OT 1:2 nanoparticles

The relatively bulky nature of the branched OT molecule (Figure 31) hinders it from forming well-packed SAMs and thus we would not expect them to be able to form ripple structure.

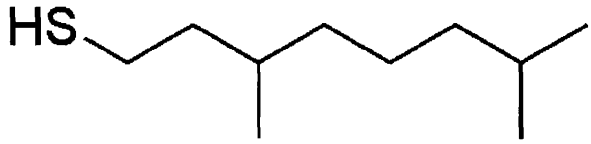

Figure 31. Schematic of the branched OT molecule.

TEM data for the MUS:branched OT 1:2 nanoparticles are shown in Figure 32. I prepared the MUS:branched OT 1:2 nanoparticles for STM in the same way I prepared the other nanoparticles. The images I have acquired suggest that their ligands are not organized as ripples, but they do exhibit some interesting structure that is not indicative of perfect mixing of the two ligands. Frequently I have observed rather deep holes or pits in the ligand shell that resemble etch pits to some extent (Figure 33). The holes are often surrounded by a raised region, resulting in donut-like shapes. Perhaps the bulkiness of the branched OT combined with the MUS make it difficult for the ligands to pack around the 3-D core of the nanoparticle without hole-like defects. Like the MUS:OT 1:2 and MUS:OT 2:1 nanoparticles, phase separation is taking place but the domains exhibit a more random organization than on rippled nanoparticles.

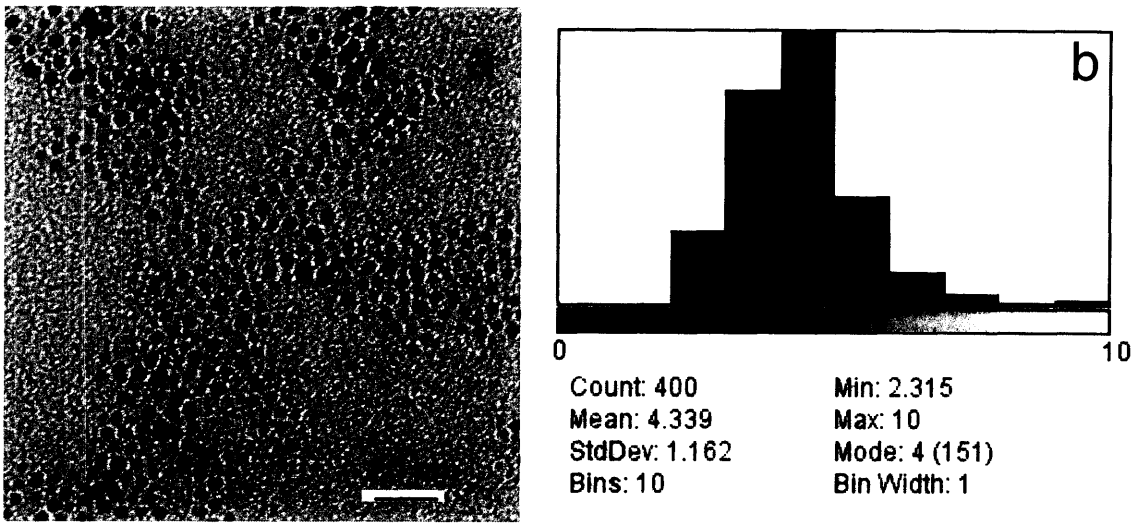

Figure 32. (a) TEM micrograph of the MUS: branched OT 1:2 nanoparticles (b) Size distribution analysis of MUS:branched OT 1:2 nanoparticles. Average particle diameter is 4.33 ± 1.16 nm, with 400 particles counted.

Assuming that the higher portions of the ligand shell in the STM images are the longer MUS molecule (which we can infer from the monolayer data, as discussed in section 5.4), these MUS:branched OT nanoparticles have worm-like domains of MUS surrounding large "holes" of hydrophobic OT.

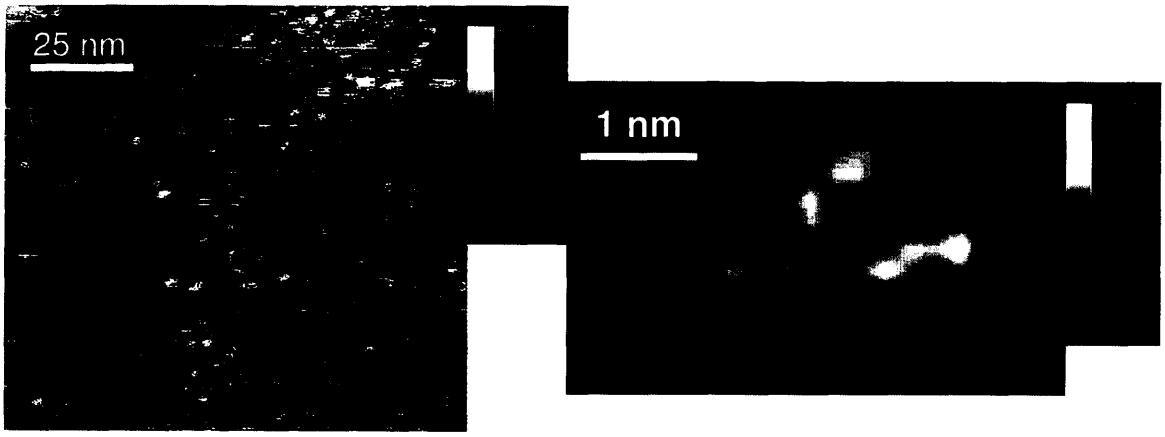

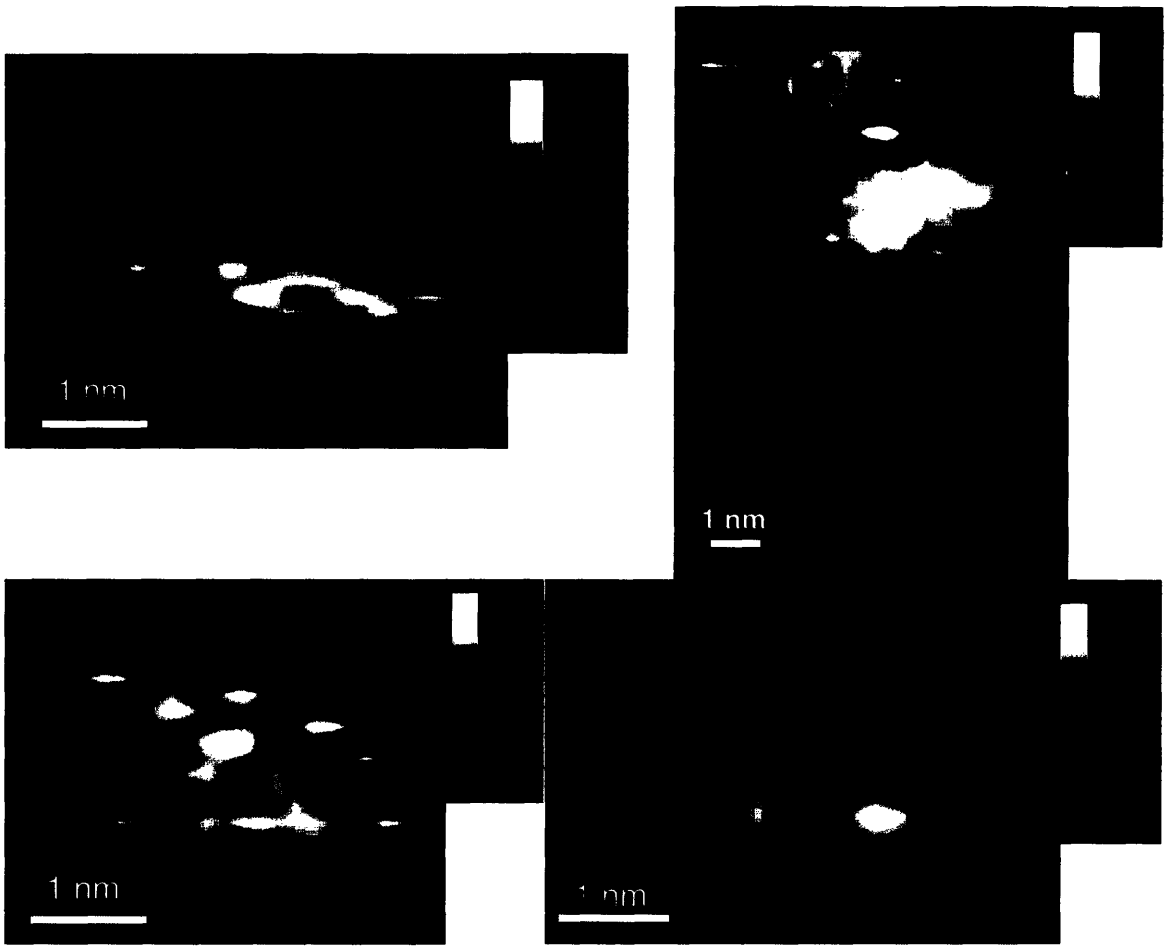

Figure 33. STM height images of MUS:branched OT nanoparticles prepared in a water:methanol 1:1 mixture and dropcast on heated bare Au(111) on mica.

The very interesting structure of these MUS:branched OT nanoparticles will require further investigation.

5.4 Monolayer Studies

In order to better understand the organization of molecules in the three-dimensional ligand shell of the nanoparticles, I investigated two-dimensional mixed monolayer formation of MUS and OT on gold on mica. I started with an all OT monolayer as a control as shown in Figure 34.

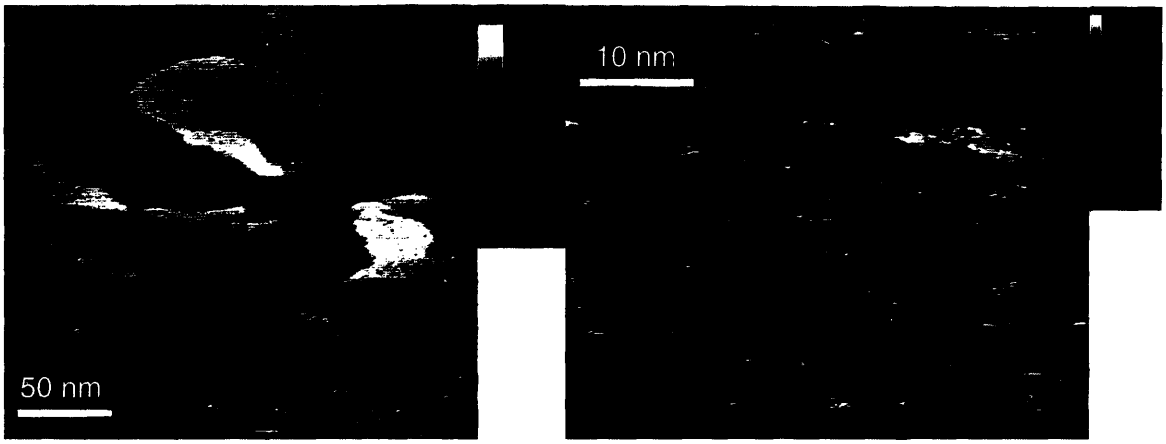

Figure 34. STM height images of octanethiol (OT) SAMs on Au (111) on mica.

I then imaged increasing proportions of MUS. All monolayers were prepared in the same manner.

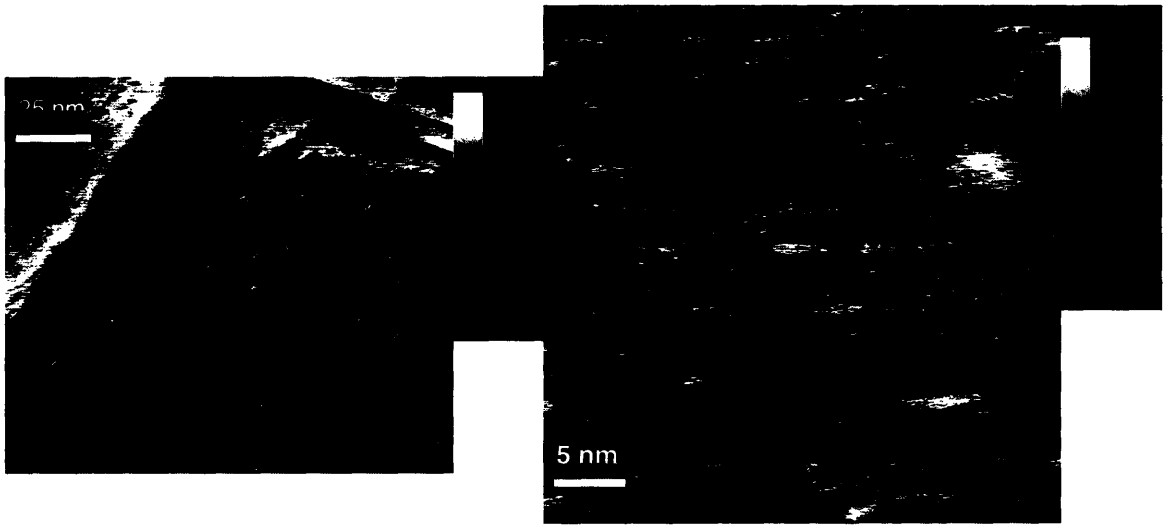

Figure 35. STM height images of MUS:OT 1:10 SAMs on Au (111) on mica. The lighter portions are believed to be the MUS molecule.

MUS:OT 1:5 monolayers on gold (Figure 36) show some etch pits that are probably due to the presence of the OT molecule, as well as some higher regions ranging from 2-6 nm in area that are probably regions of MUS molecule. There is an increased amount of streakiness due to the imaging of the MUS. The etch pits appear shallower, perhaps due to the MUS interfering with the ability of OT to form a well-packed SAM.

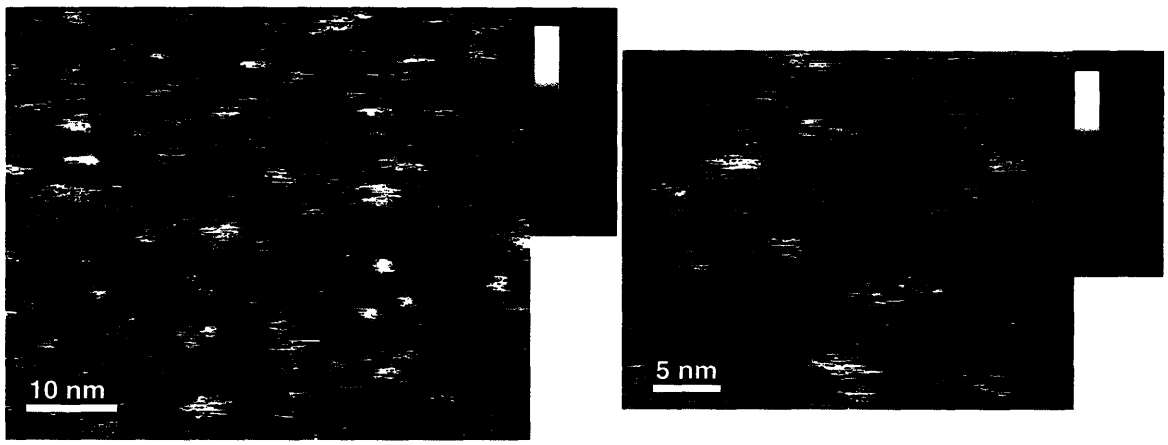

Figure 36. STM height images of MUS:OT 1:5 monolayer on Au(111) on mica. Note the increased proportion of lighter (i.e., higher) regions as compared to MUS:OT 1:10 due to the increased proportion of MUS.

I have also imaged MUS:OT 1:2 monolayers as shown in Figure 37, which are even more streaky and difficult to image.

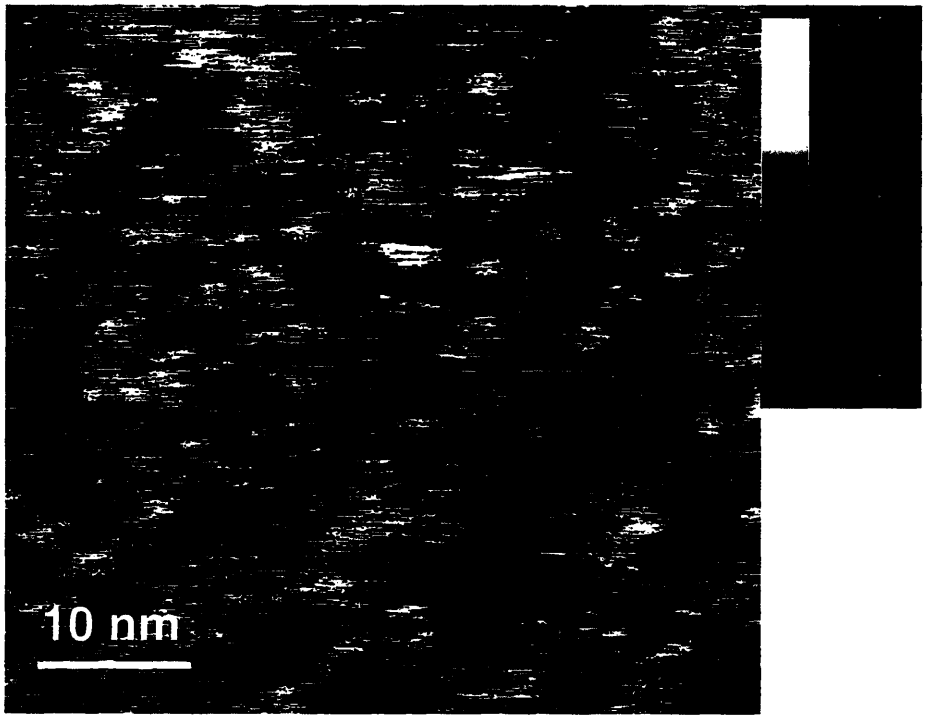

Figure 37. STM height image of MUS:OT 1:2 monolayer on bare Au (111). Domains are 1-2 Å in height.

I examined all-MUS monolayers on gold on mica, but it was very difficult to image and was very streaky. It is possible that the long length of the ligand made STM imaging difficult. I tried to use the low-current STM head as well but I have so far been

unsuccessful in getting a good image. Another explanation is that there is water trapped in the extremely hydrophilic monolayer, which will also interfere with imaging.

It is difficult to prove that the composition on the surface of the gold is in the same molar ratio as the composition of the solution from which it is made. In fact, this is probably not exactly the case since OT and MUS will interact with the solvent differently, thus affecting their affinity for the gold surface. I leave the gold soaking in the thiol solution long enough that kinetics probably does not play a role. However, assuming that the inherent affinity of the two molecules for the gold is similar, it is possible to assume that the ratio of MUS and OT on gold is similar to that in solution. Again, the monolayer sample was rather difficult to image due to streaking (most likely caused by the presence of the MUS), but I do observe areas that appear to be domains of MUS in a matrix of OT.

I also imaged a monolayer of all branched OT on gold on mica (Figure 38). There are some etch pits present, but it is clearly completely different than a SAM made up of regular OT as shown in Figure 34. The etch pits are much shallower and irregularly shaped.

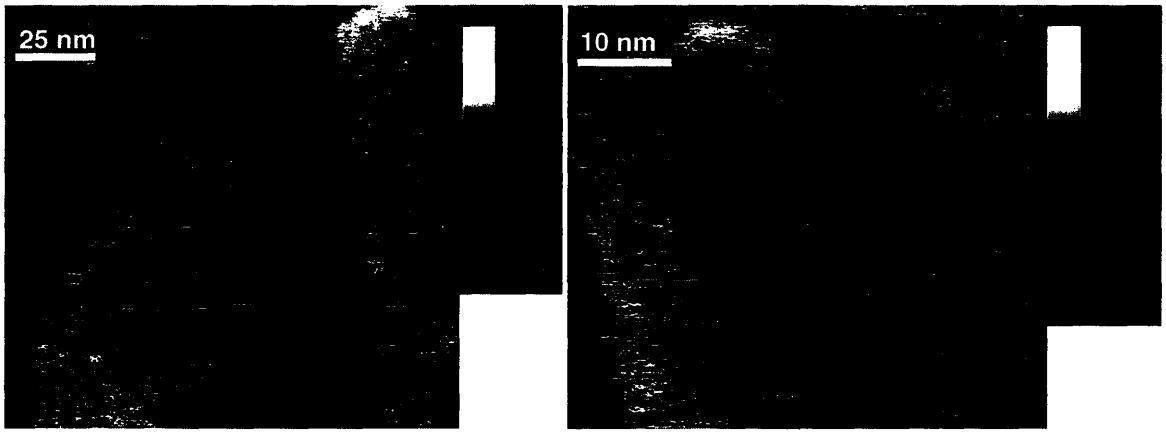

Figure 38. STM height images showing a branched OT monolayer on Au(111) on mica.

We learn several things from these monolayer studies. Firstly, the more MUS present, the more difficult it is to STM the monolayer; this obviously means that the imaging of nanoparticles containing MUS is similarly difficult. These studies also show that when MUS and OT are mixed on a two-dimensional surface, the two molecules undergo phase separation. Finally, these studies confirm that the higher, brighter domains are indeed the MUS molecule while the lower, darker phase is OT.

5.5 Imaging

The regular STM head has allowed me to image nanoparticles, but is less successful when imaging the monolayers. I have used the low-current STM head to image many of these samples. A lower set current should keep the STM tip further from the sample and thus prevent the tip from burrowing within the molecules. So far I have achieved nice images of the gold substrate or the gold covered with SAMs, but I have yet to see the low-current head provide good images of the nanoparticles themselves. I have

seen puffy-looking nanoparticle-like structures, but do not see any actual features. It is possible that the long 11-carbon chain of the MUS is mobile enough to mask the presence of the OT, and that the only way to see the phase domains of MUS and OT is to use a higher current. However, the low-current head does work well for the monolayer studies.

A final important and interesting observation is the fact that the nanoparticles are only visible under relatively large negative biases.

6 Future Work

Although dropcasting on a heated gold substrate works reasonably well for all the water soluble nanoparticles, it is still rather difficult to achieve reproducible results. The nanoparticles are heterogeneously distributed on the surface and locating optimally imageable areas requires an optical microscope as well as experience. More work can be done to try to form well-packed films of these water-soluble nanoparticles to better characterize their ligand shell morphology.

Additionally, the observation of how these nanoparticles are taken up in cells has yielded some interesting results. These nanoparticles are providing clues as to how the cell membrane functions as a barrier, and the fate of these nanoparticles once inside the cell gives us clues as to how to control what goes where in the cellular compartments. If the hypothesis that the nanoparticles are forming pores in the cell membrane proves to be true, these nanoparticles could be used as facilitators for drug delivery, providing a route of entrance for the drug delivery vehicle. More work needs to be done on how these sulfonated nanoparticles are interacting with cells and to pinpoint the role of the ligand shell composition and morphology.

7 Conclusions

In this study I have shown that it is possible to create ripple structure in water-soluble nanoparticles, and that certain composition ratios exhibit interesting organization of molecules in their ligand shell. The question of how molecules are arranged in the ligand shell is clearly not a simple one. Nanoparticles cannot be classified as "rippled" or "non-rippled"; there is indeed a wide range of structures that can be formed with varying degrees of organization. I have found a new morphological feature in ligand shells consisting of holes that may be a ligand shell packing defect. I have also demonstrated a novel and versatile sample preparation method that can yield molecular-level resolution STM images for a range of water-soluble nanoparticles.

How the structure of the ligand shell of these nanoparticles effect cellular uptake remains to be seen, but it is highly probable that the arrangement of ligands plays an important role. Results have shown that MUS:OT 2:1 and MUS:OT 1:2 nanoparticles are taken up by cells, yet all-MUS and MUS:branched OT 1:2 nanoparticles are not. This phenomenon cannot be explained by ligand shell composition and chemistry alone. This result leads us to believe that the relative position of molecules in the ligand shell of the nanoparticles does indeed have an effect on how nanoparticles interact with biological systems.

More studies will have to be done to determine conclusively the configuration of the molecules in the ligand shell of these nanoparticles, and correlate this information to

cell uptake data. This new family of water-soluble nano-structured nanomaterials may demonstrate new properties due to the unique structure in their ligand shell.

(1) Verma, A.; Simard, J. M.; Rotello, V. *Abstr Pap Am Chem S* **2004**, *228*, U92-U92.

(2) Pasquato, L.; Rancan, F.; Scrimin, P.; Mancin, F.; Frigeri, C. *Chem Commun* **2000**, 2253-2254.

(3) Demers, L. M.; Mirkin, C. A.; Mucic, R. C.; Reynolds, R. A.; Letsinger, R. L.; Elghanian, R.; Viswanadham, G. *Anal Chem* **2000**, *72*, 5535-5541.

(4) El-Sayed, I. H.; Huang, X. H.; El-Sayed, M. A. *Cancer Letters* **2006**, *239*, 129-135.

(5) Wagner, F. E.; Haslbeck, S.; Stievano, L.; Calogero, S.; Pankhurst, Q. A.; Martinek, P. *Nature* **2000**, *407*, 691-692.

(6) Rao, C. N. R.; Kulkarni, G. U.; Thomas, P. J.; Edwards, P. P. *Chem Soc Rev* **2000**, *29*, 27-35.

(7) Murray, C. B.; Kagan, C. R.; Bawendi, M. G. *Annu Rev Mater Sci* **2000**, *30*, 545-610.

(8) Schmid, G.; Pfeil, R.; Boese, R.; Bandermann, F.; Meyer, S.; Calis, G. H. M.; Vandervelden, W. A. *Chem Ber-Recl* **1981**, *114*, 3634-3642.

(9) Brust, M.; Walker, M.; Bethell, D.; Schiffrin, D. J.; Whyman, R. *J Chem Soc Chem Comm* **1994**, 801-802.

(10) Daniel, M. C.; Astruc, D. *Chemical Reviews* **2004**, *104*, 293-346.

(11) Templeton, A. C.; Chen, S. W.; Gross, S. M.; Murray, R. W. *Langmuir* **1999**, *15*, 66-76.

(12) Levy, R.; Thanh, N. T. K.; Doty, R. C.; Hussain, I.; Nichols, R. J.; Schiffrin, D. J.; Brust, M.; Fernig, D. G. *J Am Chem Soc* **2004**, *126*, 10076-10084.

(13) Brust, M.; Kiely, C. J. *Colloid Surface A* **2002**, *202*, 175-186.

(14) Kang, S. Y.; Kim, K. *Langmuir* **1998**, *14*, 226-230.

(15) Hostetler, M. J.; Green, S. J.; Stokes, J. J.; Murray, R. W. *J Am Chem Soc* **1996**, *118*, 4212-4213.

(16) Ingram, R. S.; Hostetler, M. J.; Murray, R. W. *J Am Chem Soc* **1997**, *119*, 9175-9178.

(17) Porter, L. A.; Ji, D.; Westcott, S. L.; Graupe, M.; Czernuszewicz, R. S.; Halas, N. J.; Lee, T. R. *Langmuir* **1998**, *14*, 7378-7386.

(18) Tzhayik, O.; Sawant, P.; Efrima, S.; Kovalev, E.; Klug, J. T. *Langmuir* **2002**, *18*, 3364-3369.

(19) Templeton, A. C.; Wuelfing, M. P.; Murray, R. W. *Accounts Chem Res* **2000**, *33*, 27-36.

(20) Nakamura, K.; Kawabata, T.; Mori, Y. *Powder Technol* **2003**, *131*, 120-128.

(21) Cleveland, C. L.; Landman, U.; Shafigullin, M. N.; Stephens, P. W.; Whetten, R. L. *Z Phys D Atom Mol Cl* **1997**, *40*, 503-508.

(22) Leff, D. V.; Ohara, P. C.; Heath, J. R.; Gelbart, W. M. *Abstr Pap Am Chem S* **1995**, *209*, 20-Phys.

(23) Terrill, R. H.; Postlethwaite, T. A.; Chen, C. H.; Poon, C. D.; Terzis, A.; Chen, A. D.; Hutchison, J. E.; Clark, M. R.; Wignall, G.; Londono, J. D.; Superfine, R.; Falvo, M.; Johnson, C. S.; Samulski, E. T.; Murray, R. W. *J Am Chem Soc* **1995**, *117*, 12537-12548.

(24) Whetten, R. L.; Khoury, J. T.; Alvarez, M. M.; Murthy, S.; Vezmar, I.; Wang, Z. L.; Stephens, P. W.; Cleveland, C. L.; Luedtke, W. D.; Landman, U. *Adv Mater* **1996**, *8*, 428-&.

(25) Hostetler, M. J.; Wingate, J. E.; Zhong, C. J.; Harris, J. E.; Vachet, R. W.; Clark, M. R.; Londono, J. D.; Green, S. J.; Stokes, J. J.; Wignall, G. D.; Glish, G. L.; Porter, M. D.; Evans, N. D.; Murray, R. W. *Langmuir* **1998**, *14*, 17-30.

(26) Ulman, A.; Eilers, J. E.; Tillman, N. *Langmuir* **1989**, *5*, 1147-1152.

(27) Templeton, A. C.; Hostetler, M. J.; Kraft, C. T.; Murray, R. W. *J Am Chem Soc* **1998**, *120*, 1906-1911.

(28) Badia, A.; Cuccia, L.; Demers, L.; Morin, F.; Lennox, R. B. *J Am Chem Soc* **1997**, *119*, 2682-2692.

(29) Kiely, C. J.; Fink, J.; Brust, M.; Bethell, D.; Schiffrin, D. J. *Nature* **1998**, *396*, 444-446.

(30) Stranick, S. J.; Atre, S. V.; Parikh, A. N.; Wood, M. C.; Allara, D. L.; Winograd, N.; Weiss, P. S. *Nanotechnology* **1996**, *7*, 438-442.

(31) Smith, R. K.; Reed, S. M.; Lewis, P. A.; Monnell, J. D.; Clegg, R. S.; Kelly, K. F.; Bumm, L. A.; Hutchison, J. E.; Weiss, P. S. *J Phys Chem B* **2001**, *105*, 1119-1122.

(32) Luedtke, W. D.; Landman, U. *J Phys Chem B* **1998**, *102*, 6566-6572.

(33) Jackson, A. M.; Hu, Y.; Silva, P. J.; Stellacci, F. *J Am Chem Soc* **2006**, *128*, 11135-11149.

(34) Jackson, A. M.; Myerson, J. W.; Stellacci, F. *Nature Materials* **2004**, *3*, 330-336.

(35) Glotzer, S. C., Private communication.

(36) Fuchs, H.; Akari, S.; Dransfeld, K. *Z Phys B Con Mat* **1990**, *80*, 389-392.

(37) Schmid, M., 2006.

(38) Wooley, K. L. *J Polym Sci Pol Chem* **2000**, *38*, 1397-1407.

(39) DeVries, G. A.; Brunnbauer, M.; Hu, Y.; Jackson, A. M.; Long, B.; Neltner, B. T.; Uzun, O.; Wunsch, B. H.; Stellacci, F. *Science* **2007**, *315*, 358-361.

(40) Tatumi, R.; Fujihara, H. *Chem Commun* **2005**, 83-85.

(41) Zheng, M.; Li, Z. G.; Huang, X. Y. *Langmuir* **2004**, *20*, 4226-4235.

(42) Taton, T. A.; Mucic, R. C.; Mirkin, C. A.; Letsinger, R. L. *J Am Chem Soc* **2000**, *122*, 6305-6306.

(43) Mayer, A. B. R.; Mark, J. E. *European Polymer Journal* **1998**, *34*, 103-108.

(44) Brennan, J. L.; Hatzakis, N. S.; Tshikhudo, T. R.; Dirvianskyte, N.; Razumas, V.; Patkar, S.; Vind, J.; Svendsen, A.; Nolte, R. J. M.; Rowan, A. E.; Brust, M. *Bioconjugate Chemistry* **2006**, *17*, 1373-1375.

(45) Peng, Z. Q.; Guo, L. M.; Zhang, Z. H.; Tesche, B.; Wilke, T.; Ogermann, D.; Hu, S. H.; Kleinermanns, K. *Langmuir* **2006**, *22*, 10915-10918.

(46) Yoshizawa, K.; Iwahori, K.; Sugimoto, K.; Yamashita, I. *Chemistry Letters* **2006**, *35*, 1192-1193.

(47) Datta, K. K. R.; Eswaramoorthy, M.; Rao, C. N. R. *Journal of Materials Chemistry* **2007**, *17*, 613-615.

(48) Love, J. C.; Estroff, L. A.; Kriebel, J. K.; Nuzzo, R. G.; Whitesides, G. M. *Chemical Reviews* **2005**, *105*, 1103-1169.

(49) Bauduin, P.; Renoncourt, A.; Touraud, D.; Kunz, W.; Ninham, B. W. *Current Opinion in Colloid & Interface Science* **2004**, *9*, 43-47.

(50) Collins, K. D. *Methods* **2004**, *34*, 300-311.

(51) Centrone, A.; Hu, Y.; Jackson, A. M.; Zerbi, G.; Stellacci, F. *Small* **2007**, *3*, 814-817.

(52) Harrell, L. E.; Bigioni, T. P.; Cullen, W. G.; Whetten, R. L.; First, P. N. *Journal of Vacuum Science & Technology B* **1999**, *17*, 2411-2416.

(53) Im, J.; Lee, M.; Myung, S.; Huang, L.; Rao, S. G.; Lee, D. J.; Koh, J.; Hong, S. H. *Nanotechnology* **2006**, *17*, 3569-3573.

(54) Wang, H.; He, Y.; Ratner, B. D.; Jiang, S. Y. *Journal of Biomedical Materials Research Part A* **2006**, *77A*, 672-678.